A Deep *Hubble Space Telescope* H-Band Imaging Survey of Massive Gas-Rich Mergers[1]

S. Veilleux and D.-C. Kim

Department of Astronomy, University of Maryland, College Park, MD 20742;
veilleux@astro.umd.edu, dckim@astro.umd.edu

C. Y. Peng

Space Telescope Science Institute, 3700 San Martin Drive, Baltimore, MD 21218;
cyp@stsci.edu

L. C. Ho

The Observatories of the Carnegie Institution of Washington, 813 Santa Barbara St.,
Pasadena, CA 91101; lho@ociw.edu

L. J. Tacconi, K. M. Dasyra, R. Genzel, and D. Lutz

Max-Planck-Institut für extraterrestrische Physik, Postfach 1312, D-85741 Garching,
Germany; linda@mpe.mpg.de, dasyra@mpe.mpg.de, genzel@mpe.mpg.de, lutz@mpe.mpg.de

D. B. Sanders

Institute for Astronomy, University of Hawaii, 2680 Woodlawn Drive, Honolulu, HI 96822;
sanders@ifa.hawaii.edu

ABSTRACT

We report the results from a deep *HST* NICMOS H-band imaging survey of a carefully selected sample of 33 luminous, late-stage galactic mergers at $z < 0.3$. This program is part of *QUEST*, a comprehensive investigation of the most luminous mergers in the nearby universe, the ultraluminous infrared galaxies (ULIRGs) and the quasars (*QUEST* = *Q*uasar / *U*LIRG *E*volutionary *S*tudy). Signs of a recent galactic interaction are seen in all of the objects in the *HST* sample, including all 7 IR-excess Palomar-Green (PG) QSOs in the sample. Unsuspected double nuclei are detected in 5 ULIRGs. A detailed two-dimensional analysis of the surface brightness distributions in these objects indicates that the great majority (81%) of the single-nucleus systems show a prominent early-type morphology. However, low-surface-brightness exponential disks are detected on

large scale in at least 4 of these sources. The hosts of 'warm' (*IRAS* 25-to-60 μm flux ratio, $f_{25}/f_{60} > 0.2$), AGN-like systems are of early type and have less pronounced merger-induced morphological anomalies than the hosts of cool systems with LINER or HII region-like nuclear optical spectral types. The host sizes and luminosities of the 7 PG QSOs in our sample are statistically indistinguishable from those of the ULIRG hosts. In comparison, highly luminous quasars, such as those studied by Dunlop et al. (2003), have hosts which are larger and more luminous. The hosts of ULIRGs and PG QSOs lie close to the locations of intermediate-size ($\sim 1 - 2$ L^*) spheroids in the photometric projection of the fundamental plane of ellipticals, although there is a tendency in our sample for the ULIRGs with small hosts to be brighter than normal spheroids. Excess emission from a merger-triggered burst of star formation in the ULIRG/QSO hosts may be at the origin of this difference. Our results provide support for a possible merger-driven evolutionary connection between cool ULIRGs, warm ULIRGs, and PG QSOs. However, this sequence may break down at low luminosity since the lowest luminosity PG QSOs in our sample show distinct disk components which preclude major (1:1 – 2:1) mergers. The black hole masses derived from the galaxy host luminosities imply sub-Eddington accretion rates for all objects in the sample.

Subject headings: galaxies: active – galaxies: interactions – galaxies: Seyfert – galaxies: starburst – infrared: galaxies

1. Introduction

Galaxy merging is a key driving force of galaxy evolution. In hierarchical cold dark matter models of galaxy formation and evolution, merging leads to the formation of elliptical galaxies, triggers major starbursts, and may account for the growth of supermassive black holes and the formation of quasars (e.g., Kauffmann & Haehnelt 2000). The importance of mergers increases with redshift (e.g., Zepf & Koo 1989; Carlberg, Pritchet, & Infante 1994; Neuschaefer et al. 1997; Khochfar & Burkert 2001). It is clear that dust-enshrouded starbursts and active galactic nuclei (AGN) play an extremely important role in the high-redshift Universe and are probably the dominant contributors to the far-infrared/submm

and X-ray backgrounds, respectively (e.g., Pei, Fall, & Hauser 1999; Miyaji, Hasinger, & Schmidt 2000). These luminous, merger-induced starbursts and AGN at high redshift thus provide readily observable signposts for tracing out the main epoch of elliptical galaxy and quasar formation if the above scenario is correct.

In order to assess quantitatively the physics of the merger process and its link to the epoch of elliptical and QSO formation at high redshift we must first understand the details of galaxy merging and its relationship to starbursts and AGN in the local universe. The most violent local mergers and the probable analogs to luminous high-redshift mergers are the ultraluminous infrared galaxies (ULIRGs). ULIRGs are advanced mergers of gas-rich, disk galaxies sampling the entire Toomre merger sequence beyond the first peri-passage (Veilleux, Kim, & Sanders 2002; hereafter referred as VKS02). ULIRGs are among the most luminous objects in the local universe, with both their luminosities ($> 10^{12}$ L$_\odot$ emerging mainly in the far-IR) and space densities similar to those of quasars (e.g., Sanders & Mirabel 1996). The near-infrared light distributions in many ULIRGs appear to fit a $R^{1/4}$ law (Scoville et al. 2000; VKS02). ULIRGs have a large molecular gas concentration in their central kpc regions (e.g., Downes & Solomon 1998) with densities comparable to stellar densities in ellipticals. These large central gas concentrations (and stars efficiently forming from them) may be the key ingredient for overcoming the fundamental phase space density constraints that would otherwise prevent formation of dense ellipticals from much lower density disk systems (Gunn 1987; Hernquist, Spergel, & Heyl 1993). Kormendy & Sanders (1992) have proposed that ULIRGs evolve into ellipticals through merger induced dissipative collapse. In this scenario, these mergers first go through a luminous starburst phase, followed by a dust-enshrouded AGN phase, and finally evolve into optically bright, 'naked' QSOs once they either consume or shed their shells of gas and dust (Sanders et al. 1988a).

Gradual changes in the far-infrared spectral energy distributions between 'cool' ULIRGs (*IRAS* 25-to-60 μm flux ratio, $f_{25}/f_{60} < 0.2$), 'warm' ULIRGs, and QSOs (Sanders et al. 1988b; Haas et al. 2003) bring qualitative support to an evolutionary connection between these various classes of objects, but key elements remain to be tested. In a pilot study of a dozen ULIRGs observed with Keck and VLT, Genzel et al. (2001) and Tacconi et al. (2002) have found that ULIRGs resemble intermediate mass ellipticals/lenticulars with moderate rotation, in their velocity dispersion distribution, their location in the fundamental plane (e.g., Djorgovski & Davis 1987; Dressler et al. 1987; Kormendy & Djorgovski 1989) and their distribution of the ratio of rotation/velocity dispersion [$v_{rot} \sin(i)/\sigma$]. These preliminary results therefore suggest that ULIRGs form moderate mass ($m^* \sim 10^{11}$ M$_\odot$), but not giant ($5 - 10 \times 10^{11}$ M$_\odot$) ellipticals. A comparison between these ULIRGs and the sample of luminous radio-quiet QSOs from Dunlop et al. (2003) indicates that the ULIRGs are offset from the location of the hosts of these QSOs in the photometric projection of the fundamental

plane. The latter fall near the locale of giant ellipticals on the fundamental plane. The black hole (BH) masses inferred for the ULIRGs from the host dynamical masses and the local BH mass to bulge velocity dispersion relationship (e.g., Gebhardt et al. 2000) are akin to those of local Seyfert galaxies. From this perspective, ULIRGs and QSOs have comparable luminosities because the ULIRGs are much more efficiently forming stars and feeding their BHs at the epoch they are observed.

This pilot study (Genzel et al. 2001; Tacconi et al. 2002) has raised important questions towards understanding the evolution of ULIRG mergers and their relation to QSOs, but is limited by the small number of galaxies. For example, giant ellipticals constitute only $\sim$ 10 – 15% of all ellipticals with mass $> 10^{11}$ M$_\odot$ – a similar fraction of the most massive ULIRG hosts might have been missed in our small pilot sample. To better understand the evolutionary process of ULIRGs and their relation to elliptical galaxies and quasars, we are currently conducting a comprehensive study of a large sample of ULIRGs and QSOs which samples the full range of properties (L$_{\mathrm{IR}}$, merger state, and AGN/starburst fraction). This study is called *QUEST* (for *Q*uasar/*U*LIRG *E*volutionary *ST*udy). Our program relies on *HST* NICMOS imaging and VLT/Keck near-infrared spectroscopy to determine the structure and dynamics of ULIRG and QSO mergers, and on high-S/N *Spitzer Space Telescope* (*SST*) mid-infrared spectroscopy to quantify the energy production mechanisms in these objects, and to study their obscuration and physical conditions along the merger sequence.

The purpose of the present paper is to report the results from the *HST* NICMOS imaging component of *QUEST*. Part of the spectroscopy has been presented in Dasyra et al. (2005). In §2, we describe the *HST* sample. Next we discuss the observational strategy of our program and the methods used to obtain, reduce, and analyze the data (§3, §4, and §5, respectively). The results are presented in §6 and discussed in §7. The main conclusions are summarized in §8. Throughout this paper, we adopt $H_0 = 75$ km s^{-1} Mpc^{-1} and $q_0 = 0$ to be consistent with previous papers in this series. Given the proximity ($z < 0.27$) of all of our objects, adoption of the WMAP cosmological parameters ($\Omega_M = 0.27$, $\Omega_\Lambda = 0.73$, H$_0 =$ 71 km s^{-1} Mpc^{-1}) would not affect any of our conclusions.

2. HST Sample

The ULIRG component of *QUEST* focuses on the 1-Jy sample, a complete flux-limited sample of 118 ULIRGs selected at 60 μm from a redshift survey of the IRAS faint source catalog (Kim & Sanders 1998). The QSO component focusses on the Palomar-Green (PG) quasars of Schmidt & Green (1983). The 1-Jy ULIRGs and PG QSOs are well matched in bolometric luminosity and redshift ($z < 0.3$). Ground-based optical and near-infrared images

are available for all objects in the *QUEST* sample (e.g, Surace & Sanders 1999; Surace et al. 2001; Kim, Veilleux, & Sanders 2002; VKS02). However, many of these images, especially those from Kim et al. (2002) and VKS02, were obtained under seeing $\sim 0\rlap{.}''5 - 1\rlap{.}''0$, or $\sim 1 - 3$ kpc at $z \sim 0.15$, so the structural parameters of highly nucleated late-stage ULIRGS (i.e. objects with bright AGN or nuclear starbursts) derived from these data are uncertain. The main rationale behind our *HST* NICMOS program is to revisit these particular objects. The *HST* sample consists of 26 highly nucleated 1-Jy ULIRGs and 7 PG QSOs.[2] Table 1 lists some of the properties of these systems. We have VLT/Keck kinematic data for most of these objects. The ULIRGs in the *HST* sample were selected to have high nuclear concentration indices (ratio of the H-band luminosity from the inner 4 kpc to the total luminosity larger than $\sim 1/3$; VKS02) and the majority of them host strong, if not dominant, optical and infrared AGNs (Veilleux, Kim, & Sanders 1999a; Veilleux, Sanders, & Kim 1999b; Lutz, Veilleux, & Genzel 1999 and references therein). This subset of ULIRGs is therefore AGN biased and not representative of the 1-Jy sample as a whole. The 7 PG QSOs in the sample have IR-to-optical luminosity ratios which are similar to those of the 1-Jy ULIRGs, *i.e.* they are IR-excess QSOs with $L_{IR}/L_{BOL} > 0.4$. They were selected from the sample of Surace et al. (2001) and are probably not representative of the PG QSO sample in general. They represent a small subset of the *QUEST* QSO sample. Two of the QSOs in the *HST* sample have absolute B-band magnitudes which are significantly fainter than the traditional luminosity threshold of QSOs ($M_B = -23$ for $H_0 = 50$ km s^{-1} Mpc^{-1}; see Table 1).

3. Observational Strategy and Data Acquisition

The main observational goals of our program are to extract the central point sources from our targets and derive accurate structural parameters of the underlying hosts. The excellent spatial resolution and sensitivity of the *HST* NICMOS camera in the non-thermal infrared are best suited for these observations. NICMOS was selected over ACS to reduce the impact of dust extinction and star formation on the measurements (especially in the cores of ULIRGs; VKS02). The strong thermal background of NICMOS makes deep observations at K unrealistic; our program therefore focuses on the H band (F160W filter), roughly matching the waveband of our Keck and VLT spectra. Given the redshifts of our targets (z ~ 0.05 – 0.25) and the strengths of the emission features in these objects (see, e.g., Veilleux et al. 1999b; Genzel et al. 2001; Tacconi et al. 2002), contamination by emission lines (mainly [Fe II] and Paβ) is at most $\sim 10\%$ for the F160W filter, and is therefore not an issue here.

---

[2] Mrk 1014 is both a 1-Jy ULIRG and a PG QSO. In the present paper, we adopt the QSO classification for this object.

The need for deep images can hardly be overstated. Comparisons of our ground-based R (6400 Å) and K′ (2.1 μm) imaging of ULIRGs with the results derived from shallow (e.g., SNAP) *HST* images show that too shallow *HST* data underestimate the luminosities and half-light radii of the hosts, make profile fitting ambiguous (e.g., de Vaucouleurs versus exponential disk), and can even completely overlook low-surface-brightness exponential disks extending significantly beyond galactic bulges (e.g., see discussion in §4 in VKS02; also Peng et al. 2002). Our ground-based analysis of the 1-Jy sources shows that we need to reach detection levels of about ~ 21.5 mag. arcsec^{-2} at K′ (i.e. about 1.5 mag. arcsec^{-2} deeper than the data of VKS02) to avoid these problems. This is equivalent to ~ 21.8 mag. arcsec^{-2} at H assuming colors that are typical of elliptical galaxies at z = 0.1 – 0.2 (e.g., Lilly & Longair 1984).

The NIC2 camera was chosen for this program, based on the requirements of good sensitivity to low surface brightness features, excellent spatial resolution (0.″076 pixel^{-1}) for accurate PSF (FWHM = 0.″14) removal, and a field of view (19.″5 × 19.″5) large enough to encompass most of the structures in our targets. With this camera, the aforementioned H-band flux level is reached in ~ 45 minutes with the F160W filter. One full orbit was therefore used to acquire deep images of each target, for a total of 33 orbits. A centered 4-point spiral dither pattern (NIC-SPIRAL-DITHER) with steps of 22.5 pixels was used to better sample the instrumental PSF, and aid with the recognition and elimination of data artifacts (e.g., dead and hot pixels, unstable columns, cosmic-ray afterglow). A shorter sequence of exposures was taken at the beginning of each orbit to make full use of the orbit and reduce the impact of persistence; this sequence was not used in the final analysis. At each dither position, a logarithmic STEP64 MULTIACCUM sequence with NSAMP = 18 (except for the first sequence where NSAMP = 8-12) was used to provide the largest dynamic range and allow the calibration to recover the bright central point source. The resulting exposure time for each object is 2560 seconds. An additional orbit was used to obtain several MULTIACCUM exposure sequences of two stars (SA 107-626 and SA 107-627) and fully characterize the PSF. We find below (§5) that the stellar PSF derived from these data is adequate to remove the central point source from the objects in our sample.

4. Data Reduction

The raw *HST* NICMOS data were first processed with the IDL procedure *undopuft.pro* written by Eddie Bergeron at the STScI for removal of electronic echoes of bright source and associated stripes (known as "Mr. Stay-Puft"). These data were subsequently processed with the standard pipeline processing task *calnica* within IRAF/STSDAS. This task corrects

for the non-linearity of the detector and removes bias value, dark current, amplifier glow, and shading. Variable quadrant bias or "pedestal" that cannot be removed by *calnica* was removed using the *pedsky* task. This task also removes the sky signal from each image. A visual inspection of the data shows that this method gives excellent results even for objects which cover more than half of the field of view (F05189–2524 may be the only problem case; see §6). Data taken after the South Atlantic Anomaly (SAA) passage show cosmic ray persistence that decays with time and leaves a mottled, blotchy or streaky pattern of noise signal across the images. The IDL procedure *saa_clean.pro* was used to remove this effect. Next, the four dithered exposures of each object were combined using the "drizzle" technique (Gonzaga et al. 1998). This technique combines dithered images while preserving photometric accuracy, enhancing resolution, and correcting geometric distortion. In the same process, this technique removes cosmic rays, the central bad column, and the coronographic hole. Warm pixels are not noticeable in our data. For the photometric calibration of the reduced data, a Vega-normalized magnitude for F160W (NIC2) was derived following the recipe in the *HST* Data Handbook for NICMOS (Dickinson et al. 2002) using the calibration appropriate for Cycle 12 data obtained with warm, T = 77.1 K, detectors: $m(\mathrm{F160W}) = -2.5$ log [PHOTFNU × CR / f_ν (Vega)] $= 22.107 - 2.5$ log (CR) where PHOTFNU $= 1.49816 \times 10^{-6}$ Jy sec DN^{-1}, a keyword in the calibrated data which indicates the bandpass-averaged flux density for a source that would produce a count rate of 1 DN sec^{-1}, CR is the count rate in DN sec^{-1}, and f_ν(Vega) = 1043.5 Jy, the flux density of Vega in the F160W band for NIC2.

5. Data Analysis

The two-dimensional fitting algorithm GALFIT (Peng et al. 2002) was used to accurately remove the central point source in each object and determine the structural parameters of the underlying host. The algorithm improves on previous techniques in two areas, by being able to simultaneously fit one or more galaxies with an arbitrary number of components (e.g., Sérsic profile, exponential disk, Gaussian or Moffat functions), and with optimization in computation speed. The azimuthal shapes are generalized ellipses that can fit disky or boxy components.

In galaxy fitting it is very much a judgment call when it comes to deciding which types of components and how many components to fit. Because the studies in literature (*i.e.* our comparison sample) were mostly based on a single component Sérsic profile, or in some cases using two (*i.e.* bulge-disk decomposition), to make a sensible comparison, we have to follow the same strategy. Thus, the technique we settled on for the ULIRG/PG QSO project was

motivated by interests to: (1) compare the gross, *i.e.* average, galaxy morphology of ULIRGs and PG QSOs to the early-type galaxy population, and (2) in ULIRGs or PG QSOs where there appeared to be two components, to do a bulge-disk decomposition to isolate just the bulge for a more direct comparison with early-type galaxy properties. This meant that we did not fit all galaxies to very high detail, e.g. tidal features are fitted by unrealistic ellipsoid components.

In contrast, in Peng et al. (2002) one goal was to model galaxy profiles in detail to see whether there were sub-components embedded inside early-type galaxies. The other goal was to illustrate the capability of GALFIT for doing multi-component fitting. Therefore the goals called for using as many components as necessary to do a highly faithful decomposition, in terms of reducing the residuals down to near the noise level, even if some of the components may not be real. In our ULIRG/QSO study, we are interested only in physically meaningful components, as we understand them. But because of the complexity, we also must use quite a bit of judgment and intuition to tell us what "physically meaningful" means, instead of trying to fit everything we see in an image. However subjective, admittedly, this is the only recourse.

5.1.   One Galaxy Component Fits

The analysis of each object followed a number of well-defined steps. First, we constructed a mask to exclude bright stars or small foreground/background galaxies within the field of view. Next, we proceeded to fit the surface brightness distribution of each object using a single Sérsic component (observed intensity profile $I \propto \exp[-R^{1/n}]$) to simulate the galaxy host and a PSF model to account for the possibility of an unresolved nuclear starburst or AGN. The high-S/N PSF model was derived from our deep images of SA 107-626 as described in §3 above. SA 107-627 was found to show a suspicious shoulder near the profile core and was not used to create the PSF model. We found that this method gave virtually identical results to the use of theoretical Tiny Tim PSFs.

The Sérsic component was convolved with the PSF before comparison with the data. Three Sérsic components were examined: $n =$ free (*i.e.* left unconstrained), $n = 1$ (exponential disk profile), and $n = 4$ (de Vaucouleurs profile). In all cases, the centroids of the PSF and Sérsic components were left unconstrained. This relatively simple one galaxy component analysis allowed us to get a general sense of the complexity of each system and whether the system is disk- or spheroid-dominated.

5.2.   Two Galaxy Component Fits

The residuals from the one component galaxy fit are often quite significant. This is generally the results of merger-induced morphological anomalies. However, in other cases, these residuals may indicate the presence of a second low-surface-brightness galaxy component (e.g., disk). So we decided to look into this possibility by adding a second (PSF-convolved) galaxy component to the fits for each object and examining the effects on the goodness of the fits. We studied the following three cases: $(n = 1) + (n = \text{free})$; $(n = 4) + (n = \text{free})$; $(n = 1) + (n = 4)$. Here again, the centroids of the various components were left unconstrained. Not surprisingly given the larger number of free parameters, these two-component models generally provide better fits to the data. However, a careful examination of the fitted components often indicate that the second galaxy component is not physically meaningful.

There are usually many ways to recognize when a second galaxy component is not real or not physically meaningful. For instance, the most common symptoms of unrealistic components are when one or more parameters converge to extreme values such as: 1. Luminosity becomes too faint (implying the component is not needed), or too bright (implying the Sérsic index is too high). 2. Size becomes too small (implying PSF artifacts) or extremely large (implying sky problem or neighboring contamination). 3. Axis ratio is too small, implying PSF artifact. 4. Position mis-centered, implying peculiar morphology (e.g., merger-induced morphological anomalies) or the component has gone and fitted one of the neighbors. 5. Sérsic index n is large ($n > 4$), implying 2 or more components, PSF artifacts, neighboring contamination, sky problems, or a combination of some of these effects. Condition 5 is usually the telltale sign for multiple components. Based on experience, such systems can sometimes have bulge+disk components, if the PSF residuals are not the dominant cause for a high n. Sometimes, having a large Sérsic index also indicates there is contamination due to neighboring objects – in which case both galaxies should be fitted simultaneously to better determine the morphology of the primary object.

The surest way to recognize when a second galaxy component is real is to "put back" into the residual image the model components individually to see which structure was being fitted. The components have to be fairly distinct both spatially (e.g. axis ratio, size, centering) and morphologically (concentration) for us to accept the two components as being real in our assessment.

5.3. Binary Systems

Finally, in five systems, the residuals from both the one and two galaxy component analyses show the presence of a previously unsuspected companion galaxy separated from the main component by less than $1''$. In these cases, we limit our analysis to a one galaxy component analysis (PSF + Sérsic component) for *each* galaxy in the system, leaving the centroids and Sérsic indices unconstrained.

5.4. Independent Check on the Analysis

In some cases, the analysis was carried out a second time by other members of our group to independently verify the significance of the results. There are three aspects of the analysis that require some subjective judgment. As mentioned above, we must decide on the number of components to use and their physical realities: we do this by fitting multiple components, and examining the parameters to determine whether they are significant galaxy components that perhaps represent, for example, bulge, disk, bar, compact nuclear component. In addition, some PSF residuals due to PSF mismatch may in fact be large, thus one must decide whether the galaxy component is significantly affected (and if so, what to do about it: masking or fitting). Thirdly, in systems that appear to be highly interacting or have large tidal tails, one has to decide how to perform a decomposition: do we mask out the neighbor or fit them together, representing the tidal feature by another component. Thus this independent reanalysis by different members of our team addresses particular subtle cases that fall under one or some of these categories.

6. Results

The results from the GALFIT analysis are shown in Figures 1 – 3 and listed in Tables 2 – 4. Figure 1 presents the residuals found after subtracting one galaxy component models (PSF + Sérsic with n = free, 1, or 4) from the surface brightness distributions of single-nucleus systems in our sample. Also shown in this figure are the azimuthally-averaged radial intensity profiles for each scenario (n = free, 1, or 4) and the data. In a few cases (discussed in more detail in §6.2), we find that adding another Sérsic component significantly improves the goodness of the fits; the results of this more sophisticated two galaxy component analysis are shown in Figure 2. The structural parameters derived from the one and two galaxy component fits are listed in Tables 2 and 3, respectively. Note that the exact value of $n > 4$ is not too significant. It generally indicates the galaxy has either a strong core (e.g., bulge

– 11 –

dominated) or an extended wing (e.g. early-type galaxies or interacting/neighboring galaxies), or both. Large n can be caused by bad AGN subtraction, but we tried to minimize that likelihood by using multiple components for the core. We also tried to minimize neighboring contamination by fitting the neighbors and/or masking.

The exquisite spatial resolution of the *HST* data reveals for the first time the presence of two close ($\lesssim 1''$) H-band sources within the cores of 5 objects in our sample: F05024–1941, F11095–0238, F12072–0444[3], F16300+1558, and F21329–2346 (Fig. 3). The absolute magnitudes ($M_H < -21.5$) and disturbed morphologies of these sources seem to rule out the possibility of bright super star clusters in the hosts or foreground / background galaxies projected near the source. We conclude that these systems are genuine binaries. In addition, F00456–2904 is a wide ($\sim 21''$) binary that was already identified as such from the ground (VKS02). Our images also often show small galaxies in the vicinity of the PG QSOs, but they are considerably fainter ($\Delta M_H \gtrsim 4$ mags) than the QSO hosts. We have no data to determine if these small objects are associated or not with the QSOs, so we list the magnitudes of the objects in the notes to Table 2 but do not discuss them any further in this paper. As mentioned in §5.3, binary systems are dealt slightly differently from the other sources, fitting one galaxy component models (PSF + Sérsic n = free) for *each* nucleus. Figure 3 shows the results from these fits and Table 4 lists the linear separation between the nuclei and the structural parameters for each nucleus.

Table 5 provides a summary of the best-fitting model for each object in the sample. Binary systems are listed as "Ambiguous" in terms of morphological type, except for F00456–2904 whose primary component is of a late type and well separated from the companion. The best-fitting models listed in this table were adopted by inspecting the residuals and radial plots of Figures 1 – 3 and the reduced chi-squares, χ^2_ν, listed in Tables 2 – 4. The first of these χ^2_ν values takes into account residuals over the entire galaxy whereas the second one excludes the central portion which is affected by errors in the subtraction of the central PSF. These reduced chi-squares values should be used with caution when choosing the best fits. First, we note that they are generally significantly larger than unity so the fits are not formally very good. This is due in large part to the presence of merger-induced morphological anomalies; we return to this important point below (§6.2). We also notice that the chi-squares tend to be higher for larger, brighter, and more PSF-dominated objects. This is not unexpected given the definition of χ^2_ν, which is not normalized by the intensity, and given that the fraction

---

[3]Note that the second nucleus in F12072–0444 was first optically detected in the WFPC2 images of Surace et al. (1998) but was eventually classified as a very bright super stellar cluster based on its location in a magnitude-color diagram. The spectroscopic results of Dasyra et al. (2005) confirm the presence of two genuine nuclei in this system.

of the detector area that is free of galaxy emission is more limited for large systems than for small ones. Thus, χ_ν^2 cannot be used to compare the goodness of fits between objects. However, it is a useful quantity to compare the quality of fits for the same object.

Motivated by what historically has been done, we make a bimodal choice between preferring $n = 1$ (late-type) or $n = 4$ (early-type) and list our choice in Table 5. To make a bimodal decision based on a free Sérsic index n, we refer to studies both published (Barden et al. 2005; McIntosh et al. 2005) and unpublished (GEMS private communication, Haeussler et al. 2006). Their findings are based on computer simulations whereby pure $n = 1$ and $n = 4$ galaxies were placed into an image and recovered by fitting. They can show that $n = 1$ galaxies can be recovered quite accurately with a small scatter in n, centered around 1 ($\pm$ 0.5), whereas for $n = 4$ galaxies the scatter is considerably larger (due to degeneracies with the sky value and neighboring contamination), but centered around $n = 4$. Therefore, a cut at $n \sim 1.5$ to 2 is one good, somewhat unbiased, way to decide between galaxies with roughly early or late-type morphologies.

6.1.   Morphological Type

A prominent de Vaucouleurs-like component (Sérsic index $n \approx 4$) is detected in the great majority ($22/27 = 81\%$) of single-nucleus systems. The one galaxy component analysis indicates that a single spheroidal component often provides a good fit to the surface brightness distribution of the central portion of these galaxies. We see clear trends with *IRAS* 25-to-60 μm colors and optical spectral types: all warm Seyfert 2s, 1s, and QSOs except F05189–2524 have a prominent spheroidal component (Fig. 4). This simple morphological classification is generally consistent on a object-by-object basis with the ground-based results of Surace et al. (2001) and VKS02 (see Table 5).

The excellent sensitivity limit of our data allows us to search for the presence of faint, low-surface-brightness components in all of these objects. A faint exponential disk appears to be present in PG 1119+120 (Bulge/Disk = 2.4), PG 1126–041 (2.3), and PG 1229+204 (3.1) while lobsided or tidally-shredded "disks" are visible in F02021–2103, F05189–2524, F21219–1757, PG0007+106, PG0050+124, PG0157+001 (Mrk 1014), and PG2130+099. The results of our attempts to fit this second component as an exponential disk are listed in Table 3 and shown in Figure 2 only for those four cases where the addition of a second, $n = 1$ component improved the fit significantly and the result was physically meaningful (the disk had to be concentric with, and larger than, the bulge. In F05189–2524, the central "bulge" is very compact and has a steep $n = 1.7$ Sérsic profile). We note that the three QSOs with exponential disks have the lowest infrared and bolometric luminosities in our sample,

bringing further support for a luminosity dependence of the host morphological type among quasars (e.g., Dunlop et al. 2003 and references therein).

6.2. Strength of Tidal Features

Signs of galactic interactions such as tidal tails and bridges, lopsided disks, distorted outer isophotes, or double nuclei are visible in every single system in our sample, including all PG QSOs. The residual maps in Figures 1 – 3 are a particularly good indicator of these tidal features. In an attempt to quantify the importance of these features, we first add up the absolute values of the residuals from the one galaxy component fits over the region unaffected by the PSF subtraction. Then we normalize this quantity to the total host luminosities (including tidal features) and call it R_2 (see Tables 2 and 3). Although this quantity is sensitive to the presence of spiral structure, dust lanes, and bright star clusters, we find in our objects that R_2 is dominated by the presence of large-scale merger-induced anomalies. In Figure 5a, we plot R_2 versus the *IRAS* 25-to-60 μm colors for the objects in our sample. Warm quasar-like systems tend to have smaller residuals than the other objects in the sample. All PG QSOs and Seyfert 1 galaxies have $R_2 < 20\%$. Systems with late-type or ambiguous morphologies show larger residuals than early-type systems (Fig. 5b), qualitatively suggesting that galaxies with a prominent spheroid are in the later stages of a merger than the late-type and ambiguous systems. This is consistent with numerical simulations of major (1:1 – 2:1) mergers which typically produce elliptical-like galaxies (e.g., Barnes & Hernquist 1992; Naab & Burkert 2001, 2003; Bournaud, Combes, & Jog 2004; Bournaud, Jog, & Combes 2005). The spectroscopic results of Dasyra et al. (2005) also support the major-merger scenario. Note, however, that the three low-luminosity PG QSOs in our sample also have discernible disks; this appears to rule out major mergers for the origin of these particular systems.

6.3. Unresolved Nucleus

An unresolved point source is detected at the centers of most galaxies in our sample. This is not surprising given that the galaxies in our sample were selected on the basis of their high degree of nuclear concentration (§2). To quantify the importance of the PSF, we calculate the flux ratio of the PSF to the host, $I_{\mathrm{PSF}}/I_{\mathrm{host}}$ using the best one galaxy component model for each object. This ratio is generally less than unity, but varies widely from $\lesssim 0.01$ for F03250+1606 and F04313–1649 to ~ 8 for F07599+6508. Figure 6 clearly shows that this ratio increases as the object becomes more AGN-like, either based on its *IRAS* 25-to-60

μm color or its optical spectral type. The largest ratios are found among Seyfert 1 ULIRGs and PG QSOs, a sign that the AGN dominates the central H-band emission in these objects (see VKS02). This result does not rule out the possibility that a nuclear starburst is also contributing to the PSF emission, but this starburst does not produce the bulk of the H-band emission in the nucleus of Seyfert 1 ULIRGs and PG QSOs.

6.4.   Host Sizes and Magnitudes

Figure 7 shows the distribution of host sizes and absolute magnitudes for the objects in our sample. The average (median) half-light radii and H-band absolute magnitudes are 2.68 $\pm$ 1.40 (2.61) kpc and –24.07 $\pm$ 0.57 (–24.06) mag. for the entire sample and 2.59 $\pm$ 1.46 (1.91) kpc and –24.06 $\pm$ 0.56 (–24.05) mag. for singles only. These magnitudes correspond to $\sim 1.5 \pm 1$ M_H^*, where $M_H^* = -23.7$ mag. is the H-band absolute magnitude of a L^* galaxy in a Schechter function description of the local field galaxy luminosity function (Cole et al. 2001; VKS02). A K-S analysis shows that the hosts of the 7 PG QSOs in our sample are *not* significantly different from the hosts of the 1-Jy ULIRGs both in terms of magnitudes and sizes [P(null) = 0.6 and 0.4, respectively].

We find good agreement on an object-by-object basis when comparing these measurements with those of Surace & Sanders (1999) and Surace et al. (2001), except for PG 0007+106 where the apparent total magnitude reported by Surace et al. (11.81 mag.) is significantly brighter than ours (13.03 mag., $r \approx 4''$) and the 2MASS magnitude (12.72 mag., $r = 7''$). We suspect an error in the Surace et al. measurement. The H-band magnitudes of the ULIRG and PG QSO hosts in our sample are also quite similar on average with those measured by McLeod & McLeod (2001) in other PG QSOs. We also have three objects in common with Scoville et al. (2000): F05189-2524, F07599+6508, and Mrk 1014. In all three cases, the total magnitudes listed in this paper are consistent with ours within the uncertaities of the measurements.

An attempt is made in Figure 8 to compare the R-band measurements from VKS02 with the H-band measurements listed here. For this exercise, we correct the R-band magnitudes and surface brightnesses assuming R – H = 2.7 mag., a value that is typical for elliptical galaxies at $z \simeq 0.15$ (Lilly & Longair 1984; Fukugita et al. 1995). The sizes measured at R are directly compared with those measured at H. The hosts extracted from the *HST* data are on average smaller by ~ 2 kpc and fainter by ~ 0.7 mag. than the hosts derived from the ground-based data. Significant discrepancies in the average surface brightnesses within half-light radii are also found between the two data sets although no systematic trends are apparent (Fig. 8c). Part of the discrepancies in the size and surface brightness

measurements are probably due to radial color gradients which are well known to be present in these objects (redder colors near the nucleus; e.g., VKS02). The systematic shift in magnitudes may indicate an offset in the zero point of the *HST* F160W magnitudes relative to that of the ground-based H-band magnitudes, or perhaps the assumed elliptical-like R – H color is too red for the hosts of these star-forming objects. However, Figure 8*d* indicates that the importance of the central PSF is often underestimated in the ground-based data, especially among Seyfert ULIRGs with bright central point sources (e.g., F07599+6508). This confirms the suspected uncertainties associated with the PSF subtraction in the ground-based measurements of VKS02 for highly nucleated ULIRGs. The results based on the *HST* data should therefore be used for these particular objects. Systems with lower nuclear concentration do not contain strong nuclear sources so the structural parameters derived by VKS02 for these objects should be reliable.

7.   Discussion

In §1, we posed two important questions: (1) are ULIRGs elliptical galaxies in formation? (2) are ULIRGs related to QSOs? Our *HST* data provide new constraints that can help us revisit these questions. In this section, we first use the fundamental plane traced by early-type galaxies (more specifically its projection onto the photometric axes) to address these issues, and then we attempt to characterize the level of black-hole driven activity likely to be taking place in the cores of some of these sources.

7.1.   Fundamental Plane

Figure 9 shows that ULIRGs with prominent spheroids lie near the photometric projection of the fundamental plane for early-type galaxies as traced by the K-band data of Pahre (1999). However, small ULIRGs are often brighter than inactive spheroids or bulges of the same size. There are no systematic differences between the host properties of ULIRGs with Seyfert nuclei and those with LINER or H II region-like properties. The excess emission found in VKS02 in the hosts of Seyfert-1 ULIRGs was due to under-subtraction of the strong central PSF as discussed in §6.4.

Figure 9 also confirms that the hosts of the 7 PG QSOs in our sample are *not* significantly different from the hosts of the 1-Jy ULIRGs (see §6.4 for more detail). However, they appear to be smaller than the hosts of the more luminous QSOs from Dunlop et al (2003). For this comparison, we directly used the half-light radii measured from the R-band data of Dunlop

et al. (2003) without applying any color corrections, while the R-band surface brightness measurements of Dunlop et al. (2003) were shifted assuming R – H = 2.9, which is typical for early-type systems at $z \sim 0.2$ (Lilly & Longair 1984; Fukugita, Shimasaku, & Ichikawa 1995). Negative R – H radial gradients would reduce the H-band half-light radii, but the shift between the two sets of QSOs appears too large to be explained solely by this effect.

Overall, the positions of the ULIRGs and PG QSOs in our sample are consistent with those of intermediate-size ($\sim 1 - 2\ L^*$) ellipticals/lenticulars while the hosts of the luminous QSOs in the Dunlop et al. (2003) sample are more massive ellipticals. This last result is not unexpected given the correlation between black hole mass (and indirectly QSO luminosity) with galaxy mass (see §7.2 below). These results are based purely on photometry and therefore are subject to errors due to dust extinction and the presence of young stellar populations in the hosts. The tendency for the ULIRGs with small hosts to be brighter than spheroids of the same size may be attributable to excess emission from a young stellar population (Fig. 9). Nevertheless, it is comforting to see that the conclusions derived from our photometry are consistent with the kinematic results of Genzel et al. (2001) and Tacconi et al. (2002) on ULIRGs.

By and large, our results are consistent with the picture where QSO activity of moderate luminosity is triggered by galaxy mergers that result in the formation of intermediate-mass spheroids or massive bulges. The weaker merger-induced morphological anomalies found among early-type and AGN-like systems (§6.2) indicate that QSOs are indeed preferentially late stage mergers. However, one should remember that the three lowest luminosity PG QSOs in our sample also harbor a significant disk component which is difficult to explain in the context of major mergers (e.g., Naab & Burkert 2001, 2003; Bournaud, Combes, & Jog 2004; Bournaud, Jog, & Combes 2005).

7.2.   Level of Black Hole Activity

The ubiquity of supermassive black holes at the center of galaxies (e.g., Kormendy & Gebhardt 2001) suggests that black-hole driven activity is responsible for at least some of the energy emitted by the ULIRGs and QSOs in our sample. The host magnitudes derived from our data can in principle be used to derive the black hole masses in the cores of these objects, assuming the relation between black hole mass and the mass of the spheroidal component in normal galaxy (e.g., Magorrian et al. 1998; Kormendy & Gebhardt 2001; Marconi & Hunt 2003; Häring & Rix 2004) also applies to recent mergers. Using the H-band early-type host magnitude – black hole mass relation in Marconi & Hunt (2003), $\log(M_{BH}) = -2.80 - (0.464 \times M_H)$, we deduce black hole masses ranging from $\sim 10^{7.8}$ (F01004–2237

and F09539+0857) to $10^{9.0}$ M$_\odot$ (PG0157+001). The average (median) black hole mass is $\log(M_{\rm BH}) = 8.3 \pm 0.3$ (8.30). This derivation once again neglects dust extinction in the hosts (which would increase $M_{\rm BH}$) and the presence of recent or on-going star formation in the hosts (which would have the opposite effect). These photometric black hole mass estimates are similar on average with the kinematic estimates of Genzel et al. (2001) and Tacconi et al. [2002; average (median) black hole mass of $\log(M_{\rm BH}) = 7.9 \pm 0.5$ (7.6)].

Next we use these black hole masses and the bolometric luminosities of these systems to derive their Eddington ratios, *i.e.* the bolometric luminosities expressed in units of their respective Eddington luminosities. The bolometric luminosities of ULIRGs are assumed to be of order 1.15 times their infrared luminosities (e.g., Sanders & Mirabel 1996). The bolometric luminosities of the PG QSOs in our sample are calculated using the photometry of Surace et al. (2001) and Sanders et al. (1989, 1988b). In Figure 10, we see that the objects in our sample radiate at $5 - 100\%$ of the Eddington rate, assuming *all* of the energy emitted by these objects is due to AGN activity. The values derived for the H II galaxies should therefore be considered upper limits since an important fraction of their energy output probably comes from star formation rather than AGN activity. The same is probably also true for ULIRGs with LINER characteristic as discussed in Veilleux et al. (1995, 1999a), and Lutz, Veilleux, & Genzel (1999). Nevertheless it is interesting to see that the Eddington ratios measured here are similar to those measured in quasars (e.g., McLeod & McLeod 2001 and reference therein). In particular, none of the Seyferts and PG QSOs in our sample require super-Eddington accretion rates.

8. Conclusions

Our detailed two-dimensional analysis of deep *HST* NICMOS images of 26 highly nucleated 1-Jy ULIRGs and 7 PG QSOs indicates that an important fraction of them (81% of the single-nucleus systems) present early-type morphology well fit by a de Vaucouleurs-like surface brightness distribution at their centers but with significant merger-induced morphological anomalies on large scale. This provides support to the picture where ULIRGs are spheroids in formation. Their positions relative to the photometric projection of the fundamental plane for normal (non-active) spheroids are similar to those of intermediate-size ($\sim 1 - 2\ L^*$) ellipticals or lenticulars. Indeed, in a few cases, our data reveal a faint disk on large scale. However, the spheroidal components of small ULIRGs tend to be brighter than inactive spheroids of the same size. Many of these results are consistent with the kinematic data of Genzel et al. (2001) and Tacconi et al. (2002).

The host sizes, magnitudes, and surface brightness distributions of the 7 PG QSOs in

our sample are statistically identical to those of the ULIRGs. They all display significant tidal features similar to those seen in Seyfert ULIRGs, but weaker than those in H II and LINER ULIRGs. These results bring further support to the suggestion of a merger-induced evolutionary connection between ULIRGs and PG QSOs. Earlier studies that found a poor match between the host properties of ULIRGs and those of quasars used a sample of quasars which were significantly more luminous than the ULIRGs in the 1-Jy sample. However, the evolutionary sequence may break down at low luminosities: the disk components found in the lowest luminosity QSOs in our sample cannot be easily explain in the context of major mergers.

Finally, we add a note of caution when interpreting these results. The present conclusions are based purely on photometric measurements which are subject to uncertainties from dust extinction and young stellar populations. The excess emission from a young circumnuclear starburst may help explain why ULIRGs with small hosts are brighter than inactive spheroids. We are in the process of studying the kinematic properties of the objects in this sample to test our conclusions. Mid-infrared spectroscopic data from our on-going Cycle 1 *SST* program will also complement this data set by providing quantitative measurements of the evolution of the energy source — starburst versus AGN — along the merger sequence. Our *HST* data suggest that AGN-dominated ULIRGs do not require super-Eddington accretion rates.

REFERENCES

Barden, M., et al. 2005, ApJ, 635, 959

Barnes, J. E., & Hernquist, L. 1996, ApJ, 471, 115

Bournaud, F, Combes, F., & Jog, C. J. 2004, A&A, 418, L27

Bournaud, F., Jog, C. J., & Combes, F. 2005, A&A, 437, 69

Carlberg, R. G., Pritchet, C. J., & Infante, L., 1994, ApJ, 435, 540

Dasyra, K. M., et al. 2005, ApJ, in press (astro-ph/0510670).

Dickinson, M. E., et al. 2002, in HST NICMOS Data Handbook v. 5.0, ed. B. Mobasher, Baltimore, STScI

Downes, D. & Solomon, P. M. 1998, ApJ, 507, 615

Dunlop, J. S., McLure, R. J., Kukula, M. J., Baum, S. A., O'Dea, C. P., & Hughes, D. H. 2003, MNRAS, 340, 1095

Ferrarese, L., & Merritt, D. 2000, ApJ, 539, L9

Fukugita, M., Shimasaku, K., & Ichikawa, T. 1995, PASP, 107, 945

Gebhardt, K., et al. 2000, ApJ, 539, L13

Genzel, R., et al. 2001, ApJ, 563, 527

Gonzaga, S., Biretta, J. A., Wiggs, M. S. , Hsu, J. C., Smith, T. E., Bergeron, L., and the WFPC2 Group, 1998, Instrument Science Report WFPC2 98-04.

Gunn, J. E. 1987, in 'Nearby Normal Galaxies', ed. S. M. Faber (Springer), 455

Haas, M., et al. 2003, A&A, 402, 87

Hamabe, M, & Kormendy, J. 1987, IAU Symp. 127, 379

Hernquist, L., Spergel, D. N., & Heyl, J. S. 1993, ApJ, 416, 415

Kauffmann, G., & Hehnelt, M. 2000, MNRAS, 311, 576

Khochfar, S., & Burkert, A. 2001, ApJ, 561, 517

Kim, D.-C., & Sanders, D. B. 1998, ApJS, 119, 41

Kim, D.-C., Veilleux, S., & Sanders, D. B. 2002, ApJS, 143, 277

Kormendy, J., & Djorgovski, S. G. 1989, ARAA, 27, 235

Kormendy, J., & Gebhardt, K. 2001, Texas Symposium on relativistic astrophysics, 20th, held in Austin, Texas, Ed JC Wheeler and H Martel, New York, American Institute of Physics, Vol. 586, 363

Kormendy, J., & Sanders, D. B. 1992, ApJ, 388, L9

Lilly, S. J., & Longair, M. S. 1984, MNRAS, 211, 833

Lutz, D., Veilleux, S., & Genzel, R. 1999, ApJ, 517, L13

Marconi, A., & Hunt, L. K. 2003, ApJ, 589, L21

McIntosh, D. H., et al. 2005, ApJ, 632, 191

McLeod, K. K., & McLeod, B. A. 2001, ApJ, 546, 782

Miyaji, T., Hasinger, G., & Schmidt, M. 2000, A&A, 353, 25

Naab, T., & Burkert, A. 2001, ApJ, 555, L91

Naab, T., & Burkert, A. 2003, ApJ, 597, 893

Neuschaefer, L. W. et al. 1997, ApJ, 480, 59

Pahre, M. A. 1999, ApJS, 124, 127

Pei, Y. C., Fall, S. M., & Hauser, M. G. 1999, ApJ, 522, 604

Peng, C., Ho, L. C., Impey, C. D., & Rix, H.-W. 2002, AJ, 124, 266

Sanders, D. B., & Mirabel, L. F. 1996, ARA&A, 34, 749

Sanders, D. B., et al. 1988a, ApJ, 325, 74

Sanders, D. B., Soifer, B. T., Elias, J. H., Neugebauer, G., & Matthews, K. 1988b, ApJ, 328, L35

Schmidt, M., & Green, R. F. 1983, ApJ, 269, 352

Scoville, N. Z., et al. 2000, AJ, 119, 991

Surace, J. A., & Sanders, D. B. 1999, AJ, 512, 170

Surace, J. A., Sanders, D. B., & Evans, A. S. 2001, AJ, 122, 2791

Surace, J. A., Sanders, D. B., Vacca, W. D., Veilleux, S., & Mazzarella, J. M. 1998, ApJ, 492, 116

Tacconi, L. J., et al. 2002, ApJ, 580, 73

Tremaine, S., et al. 2002, ApJ, 574, 740

Veilleux, S., Kim, D.-C., & Sanders, D. B. 2002, ApJS, 143, 315 (VKS02)

Veilleux, S., Kim, D.-C., & Sanders, D. B. 1999, ApJ, 522, 113

Veilleux, S., Sanders, D. B., & Kim, D.-C. 1999, ApJ, 522, 139

Zepf, S. E., & Koo, D. C. 1989, ApJ, 337, 34

Table 1.   Sample

Name	Other Name	z	$\log\left(\frac{L_{\rm ir}}{L_\odot}\right)$	$\log\left(\frac{L_{\rm bol}}{L_\odot}\right)$	f_{25}/f_{60}	Spec. Type
(1)	(2)	(3)	(4)	(5)	(6)	(7)
F00188−0856	$\cdots$	0.128	12.33	12.39	0.143	LINER
F00397−1312	$\cdots$	0.261	12.90	12.96	0.180	HII galaxy
F00456−2904	$\cdots$	0.110	12.12	12.18	0.054	HII galaxy
F01004−2237	$\cdots$	0.118	12.24	12.30	0.288	HII galaxy
F02021−2103	$\cdots$	0.116	12.01	12.07	0.207	$\cdots$
F03250+1606	$\cdots$	0.129	12.06	12.12	0.109	LINER
F04103−2838	$\cdots$	0.118	12.15	12.21	0.297	LINER
F04313−1649	$\cdots$	0.268	12.55	12.61	0.069	LINER
F05024−1941	$\cdots$	0.192	12.43	12.49	0.132	Seyfert 2
F05189−2524	$\cdots$	0.042	12.07	12.13	0.252	Seyfert 2
F07599+6508	$\cdots$	0.149	12.46	12.52	0.314	Seyfert 1
F09039+0503	$\cdots$	0.125	12.07	12.13	0.081	LINER
F09539+0857	$\cdots$	0.129	12.03	12.09	0.104	LINER
F11095−0238	$\cdots$	0.106	12.20	12.26	0.129	LINER
F11506+1331	$\cdots$	0.127	12.28	12.34	0.074	HII galaxy
F12072−0444	$\cdots$	0.129	12.35	12.41	0.220	Seyfert 2
F12540+5708	Mrk 231	0.042	12.50	12.56	0.271	Seyfert 1
F13218+0552	$\cdots$	0.205	12.63	12.69	0.342	Seyfert 1
F14070+0525	$\cdots$	0.265	12.76	12.82	0.131	Seyfert 2
F14197+0813	$\cdots$	0.131	12.00	12.06	0.173	LINER
F15130−1958	$\cdots$	0.109	12.09	12.15	0.203	Seyfert 2
F15462−0450	$\cdots$	0.100	12.16	12.22	0.154	Seyfert 1
F16300+1558	$\cdots$	0.242	12.63	12.69	0.047	LINER
F20414−1651	$\cdots$	0.086	12.14	12.20	0.080	HII galaxy
F21219−1757	$\cdots$	0.112	12.06	12.12	0.421	Seyfert 1
F21329−2346	$\cdots$	0.125	12.09	12.15	0.073	LINER
PG0007+106[a]	III Zw 2	0.089	11.34	12.23	0.765	QSO
PG0050+124[a]	I Zw 1	0.061	11.87	12.32	0.478	QSO
PG0157+001[a]	Mrk 1014	0.163	12.53	12.68	0.243	QSO
PG1119+120[a]	Mrk 734	0.050	11.07	11.48	0.513	QSO
PG1126−041[a]	Mrk 1298	0.060	11.29	11.95	0.462	QSO
PG1229+204[a]	Mrk 771	0.063	11.05	11.69	1.853	QSO
PG2130+099[a]	Mrk 1513	0.063	11.35	11.99	0.998	QSO

Col 1: Object name. PG0157+001 is also a 1-Jy ULIRG (F01572+0009).

Col 2: Other name.

Col 3: Redshift from Kim & Sanders (1998).

Col 4: Infrared luminosity calculated using the prescription of Sanders & Mirabel (1996).

Col 5: Bolometric luminosity calculated by assuming that it is 1.15 times the infrared luminosity of ULIRGs and taken from Surace, Sanders, & Evans (2001) for PG QSOs.

Col 6: f_{25}/f_{60} flux ratio. 'Warm' objects have $f_{25}/f_{60} \geq 0.2$

Col 7: Spectral type from Veilleux, Kim, & Sanders (1999).

[a] $M_B = -22.9$ and -22.0 [PG0007+106], -23.5 and -22.6 [PG0050+124], -24.1 and -23.2 [PG0157+001], -22.3 and -21.4 [PG1119+120], -22.9 and -22.0 [PG1126−041], -22.4 and -21.5

[PG1229+204], -23.3 and -22.4 [PG2130+099] for H_0=50 km s^{-1} Mpc $^{-1}$ and H_0=75 km s^{-1} Mpc $^{-1}$, respectively.

Table 2. One Galaxy Component Fits to Single-Nucleus Systems

Name (1)	n (2)	$r_{\frac{1}{2}}$ (3)	b/a (4)	PA (5)	m_n (6)	M_n (7)	m_{PSF} (8)	M_{PSF} (9)	R_1 (10)	R_2 (11)	$\chi^2_{\nu 1}$ (12)	$\chi^2_{\nu 2}$ (13)
F00188−0856	4.0	0.90	0.90	98.5	14.32	−24.23	17.84	−20.71	9.9	7.1	4.2	3.3
	1.0	0.83	0.93	98.1	14.72	−23.83	16.53	−22.02	39.2	30.0	18.2	13.4
	4.0	0.90	0.90	98.4	14.32	−24.23	17.83	−20.72	9.7	6.9	4.3	3.3
F00397−1312	0.8	1.89	0.65	−25.7	15.83	−24.26	17.93	−22.16	29.0	23.5	6.7	5.5
	1.0	1.91	0.65	−25.7	15.81	−24.28	17.95	−22.14	27.6	23.4	6.8	5.6
	4.0	3.13	0.62	−26.1	15.53	−24.56	18.00	−22.09	42.0	38.3	10.4	9.2
F01004−2237	5.6	0.32	0.99	−4.9	15.27	−23.10	18.80	−19.57	7.2	4.6	2.3	2.2
	1.0	0.44	0.96	26.9	15.82	−22.55	16.64	−21.73	29.9	21.3	4.6	4.0
	4.0	0.37	0.98	24.7	15.39	−22.98	17.74	−20.63	9.7	5.8	2.4	2.2
F02021−2103	8.7	10.48	0.65	54.6	13.06	−25.27	17.86	−20.47	22.5	20.7	16.2	16.6
	1.0	3.44	0.67	55.7	14.00	−24.33	15.90	−22.43	42.9	31.7	49.0	31.7
	4.0	5.02	0.66	54.3	13.47	−24.86	16.54	−21.79	24.0	18.9	19.9	16.6
F03250+1606	4.1	1.66	0.73	−0.6	14.10	−24.46	$\cdots$	$\cdots$	13.9	13.9	5.5	5.5
	1.0	1.42	0.74	−0.4	14.56	−24.00	16.60	−21.96	39.8	35.0	19.3	15.1
	4.0	1.66	0.73	−0.8	14.11	−24.45	20.09	−18.47	13.5	13.1	5.5	5.5
F04103−2838	7.4	1.72	0.81	8.3	13.97	−24.40	17.07	−21.30	22.4	21.4	6.3	5.9
	1.0	1.54	0.84	12.0	14.68	−23.69	15.59	−22.78	51.8	39.7	19.3	10.8
	4.0	1.51	0.81	8.8	14.22	−24.15	16.21	−22.16	26.7	22.9	7.2	6.1
F04313−1649	4.0	3.85	0.73	84.3	15.98	−24.17	21.37	−18.78	14.7	14.6	2.9	2.9
	1.0	2.37	0.73	83.0	16.50	−23.65	18.98	−21.17	46.3	39.2	4.0	3.8
	4.0	3.77	0.74	85.0	15.97	−24.18	21.30	−18.85	16.0	15.7	2.9	2.9
F05189−2524	7.6	0.28	0.94	75.2	11.92	−24.21	12.76	−23.37	23.0	11.0	66.2	27.3
	1.0	0.41	0.93	82.2	12.57	−23.56	12.26	−23.87	47.2	28.7	154.1	110.3
	4.0	0.35	0.94	75.9	12.16	−23.97	12.49	−23.64	27.9	15.2	73.5	40.1
F07599+6508	20.0	4.72	0.96	72.8	13.53	−25.35	12.14	−26.74	61.9	9.2	27.9	4.8
	1.0	3.90	0.95	51.0	14.69	−24.19	12.08	−26.80	102.9	20.2	34.1	5.9
	4.0	4.04	0.96	50.7	14.20	−24.68	12.09	−26.79	83.9	11.1	30.3	4.5
F09039+0503	1.4	1.61	0.73	−21.0	14.77	−23.72	18.38	−20.11	34.0	32.5	14.0	13.4
	1.0	1.51	0.73	−21.8	14.85	−23.64	18.14	−20.35	37.9	35.5	15.1	14.6
	4.0	3.01	0.73	−19.4	14.40	−24.09	19.11	−19.38	33.9	32.3	16.9	16.5
F09539+0857	3.3	1.19	0.82	140.9	15.35	−23.21	17.25	−21.31	25.6	21.3	6.8	6.4
	1.0	1.17	0.84	139.8	15.81	−22.75	17.25	−21.31	44.6	33.2	13.4	8.2
	4.0	2.61	0.85	141.5	15.35	−23.21	17.25	−21.31	45.4	29.2	13.7	7.0
F11506+1331	3.6	1.35	0.79	−78.2	14.66	−23.87	18.76	−19.77	25.8	22.7	12.1	11.7

Table 2—Continued

Name	n	$r_{\frac{1}{2}}$	b/a	PA	m_n	M_n	m_{PSF}	M_{PSF}	R_1	R_2	$\chi^2_{\nu 1}$	$\chi^2_{\nu 2}$
(1)	(2)	(3)	(4)	(5)	(6)	(7)	(8)	(9)	(10)	(11)	(12)	(13)
	1.0	1.05	0.84	−62.8	15.05	−23.48	17.06	−21.47	40.9	33.7	16.9	15.4
	4.0	1.40	0.78	−78.7	14.62	−23.91	19.30	−19.23	25.3	23.1	12.1	12.0
F12540+5708	11.5	1.38	0.93	179.4	11.14	−24.99	10.57	−25.56	41.5	8.1	148.8	86.3
	1.0	1.69	0.89	170.6	12.05	−24.08	10.43	−25.70	62.1	14.2	297.0	106.5
	4.0	1.31	0.92	178.6	11.57	−24.56	10.49	−25.64	35.8	8.8	164.2	74.0
F13218+0552	5.5	4.56	0.86	−173.1	14.83	−24.74	14.62	−24.95	27.1	13.0	5.5	3.6
	1.0	3.44	0.87	175.5	15.43	−24.14	14.53	−25.04	49.9	31.5	7.4	3.9
	4.0	4.12	0.86	−173.7	14.95	−24.62	14.60	−24.97	27.1	14.6	5.6	3.5
F14070+0525	4.2	3.58	0.83	−20.6	15.40	−24.73	19.31	−20.82	19.6	18.9	5.1	4.5
	1.0	2.67	0.82	−22.3	15.86	−24.27	18.08	−22.05	37.5	34.5	7.0	4.6
	4.0	3.38	0.83	−20.4	15.43	−24.70	19.31	−20.82	20.0	19.3	4.6	4.5
F14197+0813	2.0	2.00	0.88	176.2	14.57	−24.03	17.43	−21.17	20.2	17.5	12.1	10.2
	1.0	1.69	0.91	178.3	14.78	−23.82	17.12	−21.48	31.6	28.3	15.5	13.0
	4.0	2.72	0.89	176.3	14.32	−24.28	18.23	−20.37	20.2	15.2	14.3	12.0
F15130−1958	12.7	2.00	0.78	−78.2	14.14	−24.06	15.70	−22.50	17.5	14.2	8.0	6.2
	1.0	1.71	0.74	−80.0	15.09	−23.11	15.04	−23.16	38.3	28.0	13.9	6.6
	4.0	1.51	0.77	−79.3	14.64	−23.56	15.27	−22.93	21.5	18.9	8.9	5.9
F15462−0450	12.2	24.42	0.86	−119.0	13.45	−24.56	14.24	−23.77	27.1	17.0	9.8	6.4
	1.0	3.38	0.72	−118.9	14.81	−23.20	14.12	−23.89	40.3	23.0	13.0	7.3
	4.0	5.20	0.83	−118.5	14.25	−23.76	14.18	−23.83	28.8	15.5	9.6	6.1
F20414−1651	1.7	1.42	0.43	−122.7	14.41	−23.27	17.32	−20.36	24.8	19.7	12.6	8.5
	1.0	1.28	0.43	−121.9	14.52	−23.16	17.53	−20.15	30.9	26.0	13.8	11.9
	4.0	2.10	0.43	−123.4	14.20	−23.48	17.32	−20.36	25.5	18.3	20.2	13.0
F21219−1757	11.1	8.76	0.84	130.1	12.93	−25.33	13.27	−24.99	21.0	6.8	14.8	5.7
	1.0	3.10	0.91	103.8	13.96	−24.30	13.12	−25.14	43.1	14.5	31.7	11.2
	4.0	3.91	0.86	129.4	13.46	−24.80	13.19	−25.07	23.9	6.4	16.1	5.6
PG0007+106[a]	5.6	4.22	0.90	140.3	13.62	−24.14	13.64	−24.12	28.5	15.2	9.7	4.0
	1.0	2.49	0.91	131.4	14.32	−23.44	13.56	−24.20	52.1	32.9	18.8	9.0
	4.0	3.42	0.90	139.9	13.79	−23.97	13.62	−24.14	30.0	16.2	9.8	4.0
PG0050+124	4.0	1.84	0.83	36.7	12.33	−24.61	12.24	−24.70	36.0	9.5	106.8	14.0
	1.0	1.85	0.85	34.1	12.79	−24.15	12.14	−24.80	52.6	15.9	159.0	33.2
	4.0	1.84	0.83	36.6	12.34	−24.60	12.24	−24.70	36.0	9.5	106.8	14.0
PG0157+001[a]	17.0	5.47	0.93	−40.0	13.06	−26.01	14.08	−24.99	22.2	13.4	14.5	8.6
	1.0	2.89	0.90	111.1	14.26	−24.81	13.65	−25.42	56.5	35.0	38.6	19.2

Table 2—Continued

Name	n	$r_{\frac{1}{2}}$	b/a	PA	m_n	M_n	m_{PSF}	M_{PSF}	R_1	R_2	$\chi^2_{\nu 1}$	$\chi^2_{\nu 2}$
(1)	(2)	(3)	(4)	(5)	(6)	(7)	(8)	(9)	(10)	(11)	(12)	(13)
	4.0	2.80	0.94	−50.2	13.74	−25.33	13.77	−25.30	32.1	19.5	17.9	10.0
PG1119+120[a]	4.5	1.36	0.88	166.6	12.91	−23.60	13.34	−23.17	18.9	8.3	19.7	9.6
	1.0	1.08	0.99	160.5	13.46	−23.05	13.21	−23.30	43.5	24.1	47.1	24.0
	4.0	1.30	0.89	165.9	12.96	−23.55	13.32	−23.19	18.9	8.1	19.6	9.7
PG1126−041[a]	3.0	3.44	0.41	151.5	12.97	−23.93	12.35	−24.55	39.6	6.6	59.0	9.9
	1.0	2.83	0.41	152.6	13.35	−23.55	12.32	−24.58	52.4	14.0	71.6	18.2
	4.0	3.93	0.41	151.4	12.85	−24.05	12.36	−24.54	38.8	6.3	59.6	10.6
PG1229+204	4.3	5.05	0.72	27.1	12.62	−24.39	13.72	−23.29	17.9	13.0	14.7	12.1
	1.0	3.34	0.66	28.6	13.20	−23.81	13.59	−23.42	31.4	18.1	47.0	25.9
	4.0	4.78	0.72	27.2	12.66	−24.35	13.71	−23.30	18.0	12.9	14.7	12.0
PG2130+099[a]	9.8	14.52	0.62	−131.9	12.31	−24.70	12.42	−24.59	19.3	6.3	20.0	11.7
	1.0	2.92	0.61	−135.0	13.54	−23.47	12.36	−24.65	32.8	11.1	38.3	19.7
	4.0	4.14	0.62	−132.6	13.01	−24.00	12.40	−24.61	21.4	5.7	20.8	11.6

Col 1: Object name.

Col 2: Sérsic index.

Col 3: Half-light radius in kpc of Sérsic component.

Col 4: Axis ratio of Sérsic component.

Col 5: Position angle of major axis of Sérsic component.

Col 6: Apparent H magnitude of Sérsic component.

Col 7: Absolute H magnitude of Sérsic component.

Col 8: Apparent H magnitude of PSF component.

Col 9: Absolute H magnitude of PSF component.

Col 10: Absolute residuals normalized to total host galaxy flux (%).

Col 11: PSF-masked absolute residuals normalized to total host galaxy flux (%). The central PSF region brighter than 10 H mag arcsec^{-2} was masked for these calculations.

Col 12: Reduced χ^2 value.

Col 13: PSF-masked reduced χ^2 value. The central PSF region brighter than 10 H mag arcsec^{-2} was masked for these calculations.

[a] Faint galaxies are detected in the vicinity of these QSOs. The H-band absolute magnitudes of these galaxies are −20.09 (PG0007+106), −20.02 (PG0157+001), −19.66 (PG1119+120), −19.66 (PG1126−041), and −19.66 (PG2130+099).

Table 3.   Two Galaxy Component Fits to Single-Nucleus Systems

Name	n	$r_{\frac{1}{2}}$	b/a	PA	m_n	M_n	m_{PSF}	M_{PSF}	R_1	R_2	$\chi^2_{\nu1}$	$\chi^2_{\nu2}$
(1)	(2)	(3)	(4)	(5)	(6)	(7)	(8)	(9)	(10)	(11)	(12)	(13)
PG1119+120	1.0	3.52	0.41	-19.3	14.28	-22.23	13.37	-23.14	15.2	5.7	14.4	4.1
	4.0	0.71	0.87	-111.8	13.32	-23.19						
PG1126$-$041	1.0	5.44	0.38	-10.2	14.26	-22.64	12.36	-24.54	37.4	5.5	57.5	8.2
	4.0	2.54	0.38	152.4	13.35	-23.55						
PG1229+204	1.0	6.03	0.27	124.2	14.35	-22.66	13.73	-23.28	13.8	9.8	10.8	8.9
	4.0	2.70	0.91	-10.8	13.11	-23.90						
F05189$-$2524[a]	1.7	0.29	0.94	81.1	12.46	-23.67	12.39	-23.74	9.1	3.1	34.2	8.3
	0.8	3.88	0.91	52.2	13.29	-22.84						

Col 1: Object name.

Col 2: Sérsic index.

Col 3: Half-light radius in kpc of Sérsic component.

Col 4: Axis ratio of Sérsic component.

Col 5: Position angle of major axis of Sérsic component.

Col 6: Apparent H magnitude of Sérsic component.

Col 7: Absolute H magnitude of Sérsic component.

Col 8: Apparent H magnitude of PSF component.

Col 9: Absolute H magnitude of PSF component.

Col 10: Absolute residuals normalized to total host galaxy flux (%).

Col 11: PSF-masked absolute residuals normalized to total host galaxy flux (%). The central PSF region brighter than 10 H mag arcsec^{-2} was masked for these calculations.

Col 12: Reduced χ^2 value.

Col 13: PSF-masked reduced χ^2 value. The central PSF region brighter than 10 H mag arcsec^{-2} was masked for these calculations.

[a] Note that a very compact "bulge" with $n = 1.7$ is detected in this object. This object is classified as late type in the text and all of the figures.

Table 4.   One Galaxy Component Fits to Binary Systems

Name (1)		NS (2)	n (3)	$r_{\frac{1}{2}}$ (4)	b/a (5)	PA (6)	m_n (7)	M_n (8)	m_{PSF} (9)	M_{PSF} (10)	R_1 (11)	R_2 (12)	$\chi^2_{\nu 1}$ (13)	$\chi^2_{\nu 2}$ (14)
F00456−2904	NE	20.7	5.1	5.52	0.84	−91.5	16.23	−21.99	21.35	−16.87	22.5	21.1	0.8	0.7
	SW		1.8	1.85	0.94	101.0	14.02	−24.20	16.74	−21.48	17.3	16.8	11.6	10.3
F05024−1941	NE	3.0	17.8	5.49	0.82	−89.7	14.78	−24.65	17.75	−21.68	11.7	9.8	4.0	3.6
	SW		1.8	3.20	0.45	−79.1	15.61	−23.82	20.43	−19.00				
F11095−0238	NE	0.9	2.3	1.67	0.72	−150.9	15.59	−22.55	18.52	−19.62	22.5	20.1	4.3	4.2
	SW		3.7	1.45	0.53	−162.9	16.25	−21.89	18.89	−19.25				
F12072−0444	N	2.0	14.7	10.88	0.80	−154.4	14.76	−23.80	18.04	−20.52	22.5	19.1	8.6	6.4
	S		0.4	3.58	0.79	−172.9	14.75	−23.81	17.14	−21.42				
F16300+1558	N	4.4	1.2	3.50	0.38	−42.2	16.70	−23.23	22.11	−17.82	24.2	23.8	4.2	4.2
	S		2.2	4.27	0.73	150.4	15.19	−24.74	20.06	−19.87				
F21329−2346	NE	2.4	3.5	2.67	0.60	172.4	15.03	−23.46	19.39	−19.10	14.2	13.8	4.8	4.7
	SW		1.2	0.59	0.77	119.9	16.96	−21.53	20.88	−17.61				

Col 1: Object name.

Col 2: Nuclear Separation in kpc.

Col 3: Sérsic index.

Col 4: Half-light radius in kpc of Sérsic component.

Col 5: Axis ratio of Sérsic component.

Col 6: Position angle of major axis of Sérsic component.

Col 7: Apparent H magnitude of Sérsic component.

Col 8: Absolute H magnitude of Sérsic component.

Col 9: Apparent H magnitude of PSF component.

Col 10: Absolute H magnitude of PSF component.

Col 11: Absolute residuals normalized to total host galaxy flux (%).

Col 12: PSF-masked absolute residuals normalized to total host galaxy flux (%). The central PSF region brighter than 10 H mag arcsec^{-2} was masked for these calculations.

Col 13: Reduced χ^2 value.

Col 14: PSF-masked reduced χ^2 value. The central PSF region brighter than 10 H mag arcsec^{-2} was masked for these calculations.

Table 5.   Summary[a]

Name (1)		M_{PSF} (2)	M_{host} (3)	M_{model} (4)	M_{total} (5)	$\frac{I_{PSF}}{I_{host}}$ (6)	$\frac{I_{model}}{I_{host}}$ (7)	$r_{\frac{1}{2}}$ (8)	$<\mu_{\frac{1}{2}}>$ (9)	MC (10)	MC-V02 (11)	IC (12)
F00188−0856		−20.72	−24.19	−24.23	−24.23	0.04	1.04	0.90	14.60	E	E	V
F00397−1312		−22.14	−24.35	−24.28	−24.48	0.13	0.94	1.91	16.43	A	E/D	V
F00456−2904		⋯	⋯	⋯	⋯	⋯	⋯	⋯	⋯	L, A	⋯	IIIa
	NE	−16.87	−21.80	−21.99	−21.81	0.00	1.19	5.26	20.63	A	⋯	⋯
	SW	−21.48	−24.23	−24.20	−24.31	0.08	0.97	1.76	16.32	L	E	⋯
F01004−2237		−20.63	−23.02	−22.98	−23.13	0.11	0.96	0.37	14.27	E	E/D	V
F02021−2103		−21.79	−24.72	−24.86	−24.79	0.07	1.14	5.02	17.09	E+L?	E	IVa
F03250+1606		−18.47	−24.42	−24.45	−24.42	0.00	1.03	1.66	15.41	E	E	IVb
F04103−2838		−22.16	−24.25	−24.15	−24.40	0.15	0.91	1.51	15.56	E	A	IVb
F04313−1649		−18.85	−23.99	−24.18	−24.00	0.01	1.19	3.77	17.85	E	E/D	IVa
F05024−1941		−23.30	−24.49	−24.38	−24.80	0.33	0.90	3.76	17.63	A, A	E/D	IIIb
	NE	−21.68	⋯	−24.65	⋯	⋯	⋯	5.49	18.18	A	⋯	⋯
	SW	−19.00	⋯	−23.82	⋯	⋯	⋯	3.20	17.84	A	⋯	⋯
F05189−2524		−23.74	−23.96	−24.09	−24.62	0.82	0.89	0.53	13.23	L	E	IVb
F07599+6508		−26.79	−24.55	−24.68	−26.92	7.87	1.13	4.04	17.30	E	E	IVb
F09039+0503		−20.35	−24.05	−23.64	−24.09	0.03	0.69	1.51	16.19	L	A	IVa
F09539+0857		−21.31	−22.92	−23.21	−23.14	0.23	1.31	2.61	17.76	E	E/D	V
F11095−0238		−20.26	−23.01	−22.81	−23.09	0.08	0.83	1.65	17.18	A, A	A	IIIb
	NE	−19.62	⋯	−22.55	⋯	⋯	⋯	1.67	17.46	A	⋯	⋯
	SW	−19.25	⋯	−21.89	⋯	⋯	⋯	1.45	17.80	A	⋯	⋯
F11506+1331		−19.23	−23.97	−23.91	−23.98	0.01	0.95	1.40	15.62	E	A	IVb
F12072−0444		−22.25	−24.22	−24.23	−24.38	0.16	1.01	3.65	17.53	A, A	E	IIIb
	N	−20.52	⋯	−23.80	⋯	⋯	⋯	3.58	17.91	A	⋯	⋯
	S	−21.42	⋯	−23.81	⋯	⋯	⋯	10.87	20.34	A	⋯	⋯
F12540+5708		−25.64	−24.52	−24.56	−25.97	2.81	1.04	1.31	14.65	E	E	IVb
F13218+0552		−24.97	−24.47	−24.62	−25.50	1.58	1.15	4.12	17.50	E	E	V
F14070+0525		−20.82	−24.62	−24.70	−24.65	0.03	1.08	3.38	17.22	E	E/D	V
F14197+0813		−21.48	−24.01	−23.82	−24.11	0.10	0.84	1.69	16.29	A	A	V
F15130−1958		−22.93	−23.62	−23.56	−24.08	0.53	0.95	1.51	16.05	E	E	IVb
F15462−0450		−23.83	−23.40	−23.76	−24.39	1.49	1.39	5.20	18.44	E	E/D	IVb
F16300+1558		−21.08	−24.96	−24.80	−24.99	0.03	0.86	4.10	17.52	A	E/D	IIIb
	N	−17.82	⋯	−23.23	⋯	⋯	⋯	3.50	18.75	A	⋯	⋯
	S	−19.87	⋯	−24.74	⋯	⋯	⋯	4.27	17.67	A	⋯	⋯
F20414−1651		−20.15	−23.34	−23.16	−23.40	0.05	0.85	1.28	16.21	A	E/D	IVb
F21219−1757		−25.07	−24.59	−24.80	−25.61	1.56	1.21	3.91	16.89	E+L?	E	V
F21329−2346		−19.33	−23.62	−23.72	−23.64	0.02	1.10	3.65	17.52	A, A	E	IIIb
	NE	−19.10	⋯	−23.46	⋯	⋯	⋯	2.67	17.61	A	⋯	⋯
	SW	−17.61	⋯	−21.53	⋯	⋯	⋯	0.59	16.28	A	⋯	⋯
PG0007+106		−24.14	−23.79	−23.97	−24.73	1.38	1.18	3.42	17.40	E	⋯	V
PG0050+124		−24.70	−24.53	−24.60	−25.37	1.17	1.07	1.84	15.27	E	⋯	V
PG0157+001		−25.30	−25.39	−25.33	−26.10	0.92	0.95	2.80	15.94	E	E	IVb
PG1119+120		−23.19	−23.44	−23.55	−24.07	0.79	1.11	1.30	15.62	E+L	⋯	V
PG1126−041		−24.54	−23.79	−24.05	−24.98	2.00	1.27	3.93	16.76	E+L	⋯	V
PG1229+204		−23.30	−24.06	−24.35	−24.50	0.50	1.31	4.78	17.39	E+L	⋯	V
PG2130+099		−24.61	−23.76	−24.00	−25.02	2.19	1.25	4.14	17.30	E+L?	⋯	V

Col 1: Object name.

Col 2: Absolute magnitude of PSF component.

Col 3: Absolute magnitude of host galaxy (including tidal features).

Col 4: Absolute magnitude of best-fitting galaxy host model.

Col 5: Total absolute magnitude (host + PSF).

Col 6: PSF-to-host intensity ratio.

Col 7: Model-to-host intensity ratio.

Col 8: Half-light radius in kpc of Sérsic component.

Col 9: Mean surface brightness within half-light radius in H mag. arcsec^{-2}.

Col 10: Morphological class: E = early type, L = late type, A = ambiguous. "E + L" indicates a galaxy with a dominant early-type component surrounded by an exponential disk. Question marks ("?") indicate uncertain classifications. The components in the binaries are classified as ambiguous by default, unless the components are widely separated as in the case of F00456–2904.

Col 11: Morphological class from VKS02.

Col 12: Revised interaction class based on new HST results (see VSK02 for details on the definitions).

[a] Entries in this table are the parameters from the best-fitting one galaxy component models for single objects (Table 2) and for binary systems (Table 4). As explained in §6, a bimodal choice was made between preferring $n = 1$ (late type) or $n = 4$ (early type). The only exception is F05189–2524, where the parameters from the two galaxy component fits (Table 3) were used for the calculations since the one galaxy component fit is a very poor representation of the data. The magnitudes and half-light radius of this galaxy were calculated from the sum of both components listed in Table 3. Unless otherwise noted, the figures in the paper used the entries in this table.
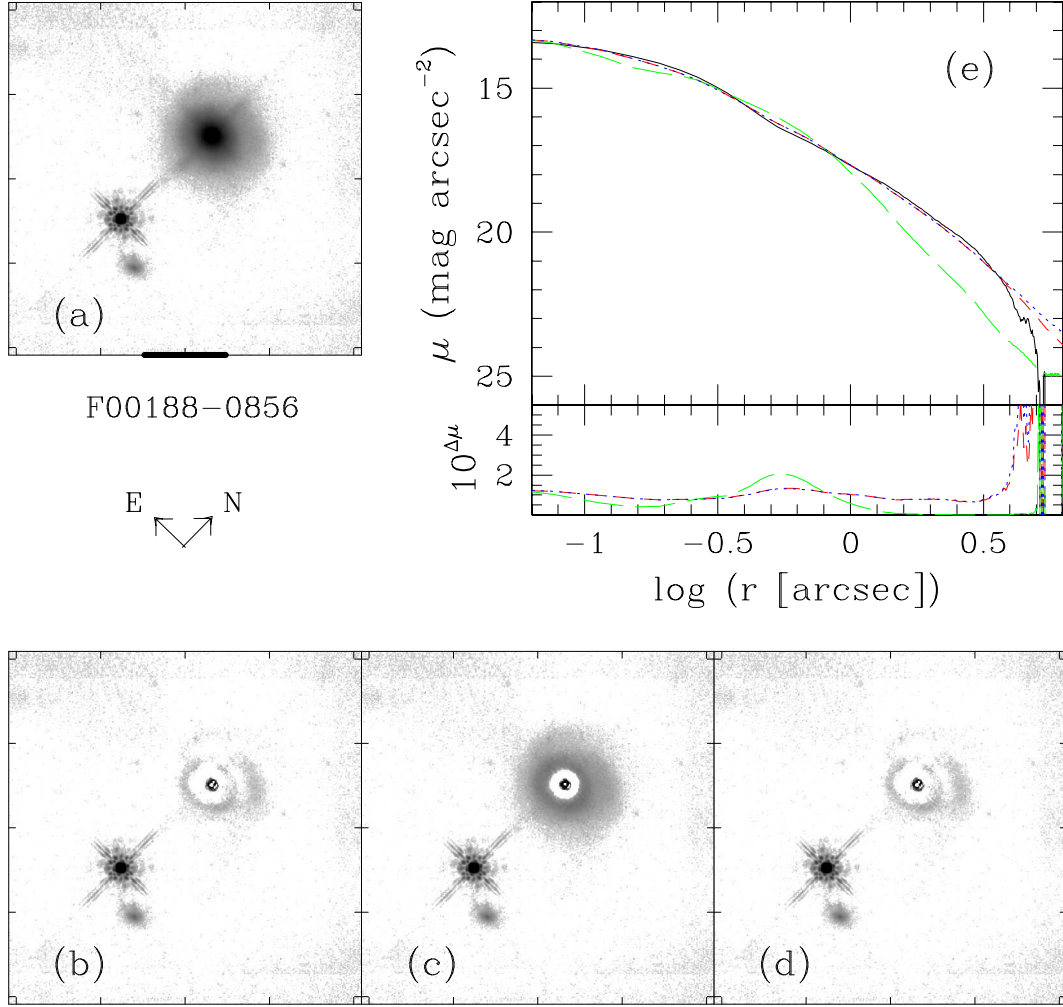
Fig. 1.— Results from the GALFIT one galaxy component analysis of single-nucleus systems. For each object, panel (*a*) shows the original data while the lower panels show the residuals after subtracting three different models: (*b*) PSF + Sérsic component with unconstrained index, (*c*) PSF + Sérsic component with $n = 1$ (exponential disk), and (*d*) PSF + Sérsic component with $n = 4$ (de Vaucouleurs spheroid). The intensity scale is logarithmic and the horizontal segment in panel (*a*) represents 10 kpc. The tickmarks in panels (a), (b), (c), and (d) are separated by $5''$. Panel (*e*) compares the observed radial surface brightness profile with those of the models: solid black line is the data, short-dashed red line is PSF + $n =$ free, long-dashed green line is PSF + $n = 1$, and dotted blue line is PSF + $n = 4$. The various PSFs used for these models are omitted for clarity. The bottom section of panel (*e*) shows the residual intensities after subtracting the models from the data.

(a)

F00397−1312

E   N

(e)

(b)   (c)   (d)

Fig. 1 –

(a)

F01004−2237

E N

(e)

μ (mag arcsec^{-2})

15

20

25

$10^{\Delta\mu}$

log (r [arcsec])

(b)

(c)

(d)

Fig. 1 –

F02021−2103

Fig. 1 –

F03250+1606

Fig. 1 –

F04103−2838

Fig. 1 –

F04313−1649

Fig. 1 –

F05189−2524

Fig. 1 –

F07599+6508

Fig. 1 –

F09039+0503

Fig. 1 –

F09539+0857

Fig. 1 –

F11506+1331

Fig. 1 –

F12540+5708

Fig. 1 –

F13218+0552

Fig. 1 –

F14070+0525

(a)

N
E

(e)

μ (mag arcsec^{-2})

$10^{\Delta\mu}$

log (r [arcsec])

(b)

(c)

(d)

Fig. 1 –

(a)

F14197+0813

N   E

(e)

μ (mag arcsec^{-2})

$10^{\Delta\mu}$

log (r [arcsec])

(b)   (c)   (d)

Fig. 1 –

F15130−1958

Fig. 1 –

F15462−0450

(a)

N

E

(e)

μ (mag arcsec^{-2})

$10^{\Delta\mu}$

log (r [arcsec])

(b)

(c)

(d)

Fig. 1 –

F20414−1651

N E

(a)

(e)

μ (mag arcsec^{-2})

15

20

25

$10^{\Delta\mu}$

6
4
2

log (r [arcsec])

−1   −0.5   0   0.5

(b)   (c)   (d)

Fig. 1 –

F21219−1757

Fig. 1 –

PG0007+106

Fig. 1 –

PG0050+124

(e)

Fig. 1 –

PG01572+001

Fig. 1 –

PG1119+120

N E

μ (mag arcsec^{-2})

$10^{\Delta\mu}$

log (r [arcsec])

(e)

Fig. 1 –

PG1126−041

Fig. 1 –

PG1229+204

Fig. 1 –

PG2130+099

N

E

(e)

Fig. 1 –

Fig. 2.— Results from the GALFIT two galaxy component analysis of single-nucleus systems. A low-surface-brightness exponential disk is detected unambiguously in only four systems. Systems with lopsided or tidally-shredded disks are not shown here because the two galaxy component analysis does not provide significantly better fits than the one galaxy component analysis for these objects. Panel (a) shows the original data and panel (b) shows the residuals after subtracting a model with a PSF, a bulge-like Sérsic component with $n = 4$, and a disk-like Sérsic component with $n = 1$. In the case of F05189–2524, the "bulge-like" component has $n = 1.7$ and the disk-like component has $n = 0.8$. Panels (c) and (d) show the surface brightness distributions of the two Sérsic components used in the model. The centroids of the components are left unconstrained. The intensity scale is logarithmic and the vertical segment between panels (b) and (c) represents 10 kpc. The tickmarks in each panel are separated by 5″.

F00456−2904

F05024−1941

F11095−0238

F12072−0444

F16300+1558

F21329−2346
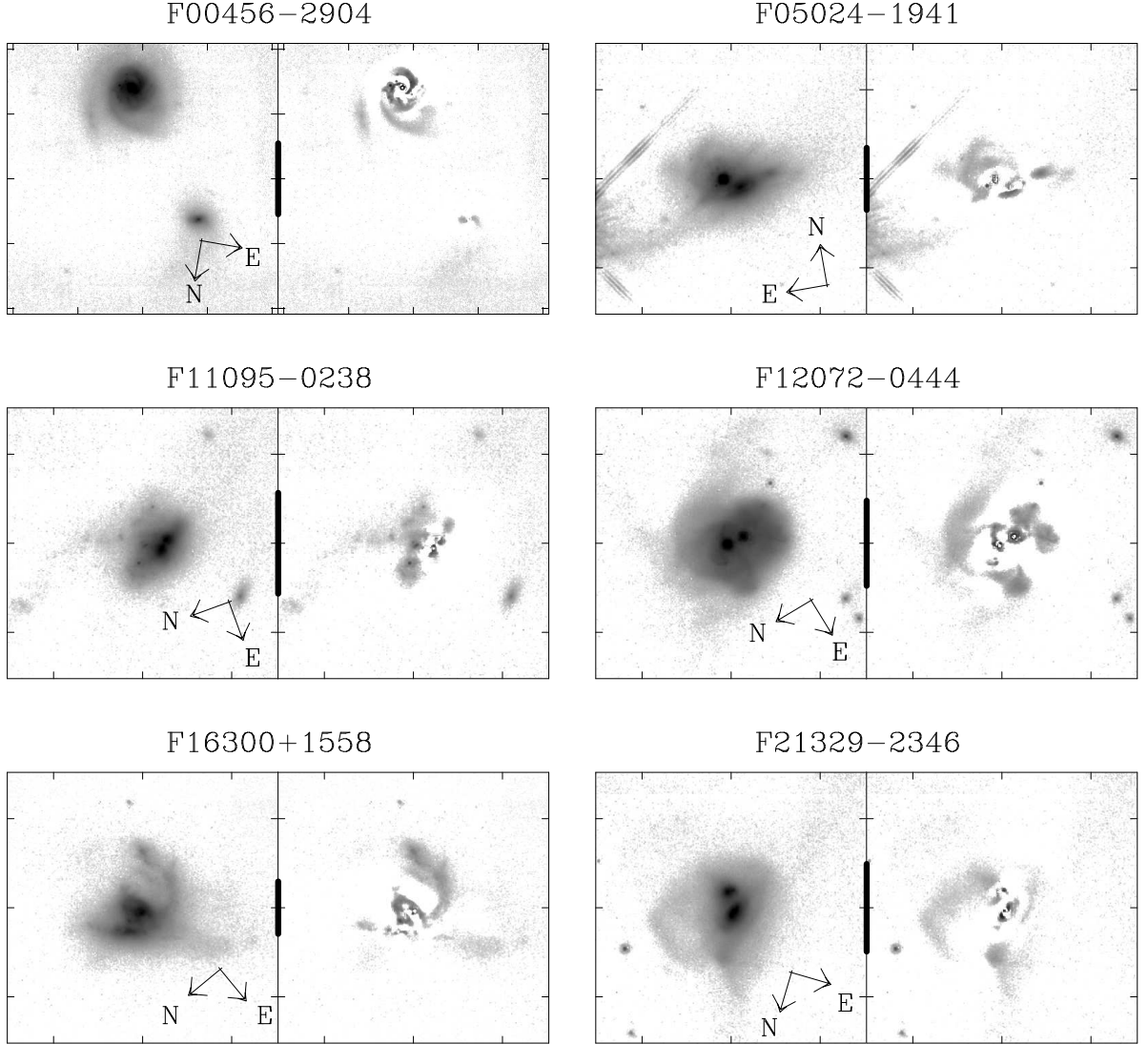
Fig. 3.— Results from the GALFIT analysis for binary systems. Panels on the left show the original data and panels on the right show the residuals after subtracting a model that assumes the sum of a PSF component and a Sérsic component with unconstrained centroid and Sérsic index for each nucleus in the system. Table 4 lists the parameters for each of these models. The intensity scale is logarithmic and the vertical segment between the panels represents 10 kpc. The tickmarks in each panel are separated by 5″.
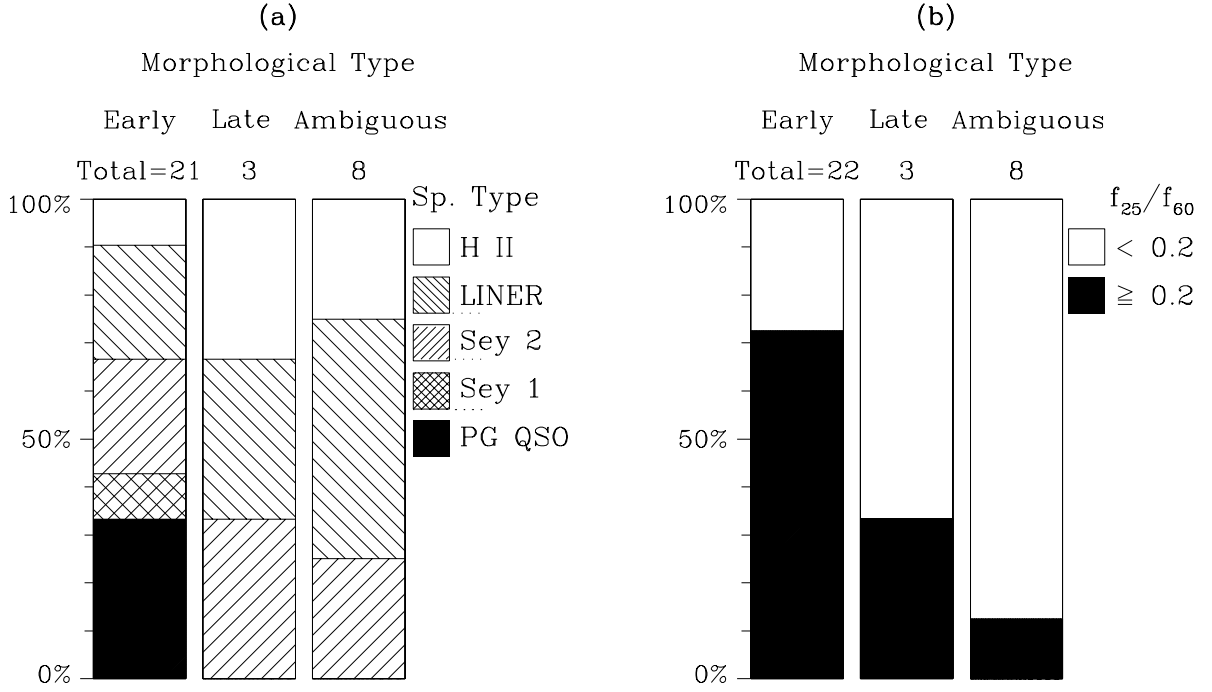
Fig. 4.— Trends between the dominant morphological types based on the one galaxy compo-
nent decomposition and (*a*) optical spectral types, (*b*) *IRAS* 25-to-60 μm colors. There is one
fewer object in panel (*a*) than in panel (*b*) because the optical spectral type of F02021−2103 is
unknown. The hosts of warm, quasar-like objects all have a prominent early-type spheroidal
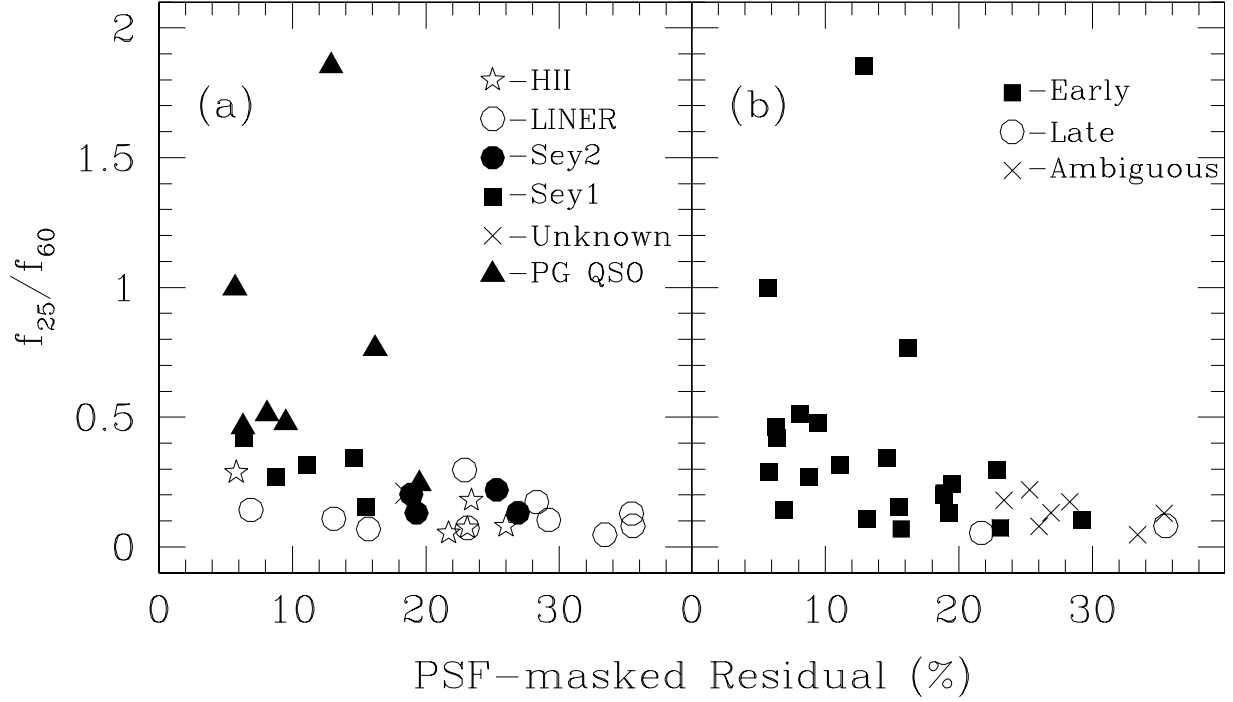component. F05189–2524 is the only Seyfert 2 ULIRG in the sample with a dominant late-
type morphology.

Fig. 5.— *IRAS* 25-to-60 μm colors plotted against the PSF-masked residuals as defined in the text. The residuals are calculated from the one galaxy component fits. F05189–2524 is not shown in these panels because a one galaxy component fit is a very poor representation of the data (see Fig. 1). The residuals are smaller among warm, quasar-like objects (*a*) with dominant early-type morphology (*b*). However, note in (*b*) that some of the quasars classified as having a dominant early-type morphology also harbour faint exponential disks on largel scale.
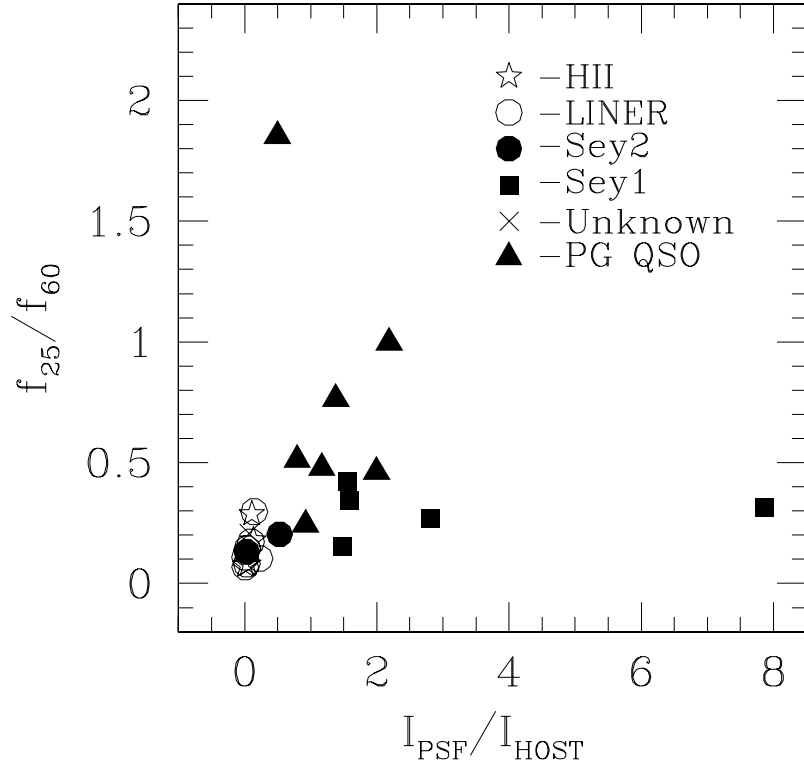
Fig. 6.— *IRAS* 25-to-60 μm colors plotted against $I_{\mathrm{PSF}}/I_{\mathrm{host}}$, the intensity of the PSF component normalized to that of the host galaxy. The object with $f_{25}/f_{100} = 1.853$ is PG1229+204, while the object with $I_{\mathrm{PSF}}/I_{\mathrm{host}} \simeq 8$ is F07599+6508. Warm, quasar-like objects have stronger PSF components than H II and LINER ULIRGs.
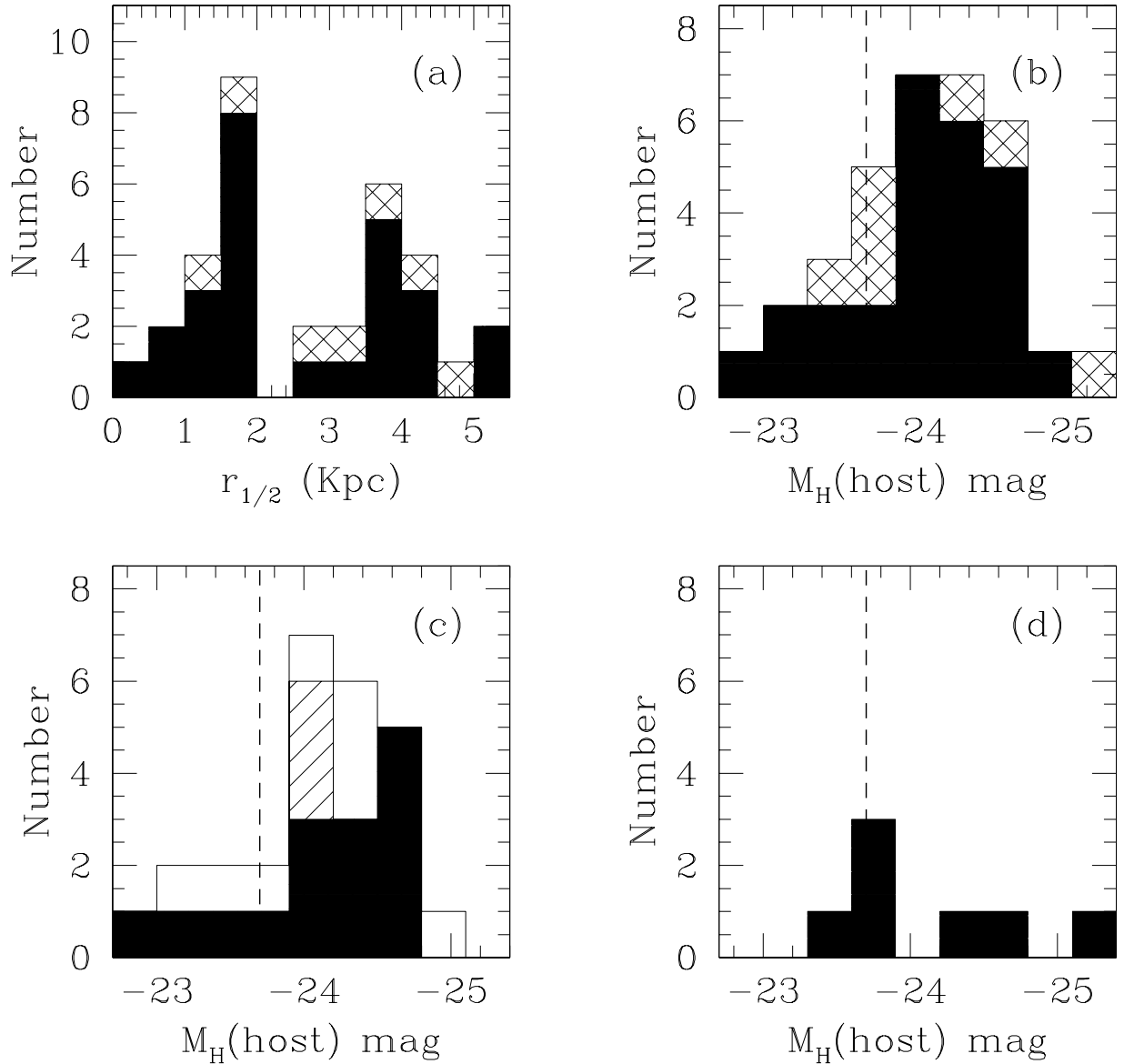
Fig. 7.— Distribution of the half-light radii and host absolute magnitudes for the objects in the *HST* sample. In panels (*a*) and (*b*), the ULIRGs are in black and the PG QSOs are cross-hatched. A K-S test on these data indicates no significant difference between the host sizes and magnitudes of the 1-Jy ULIRGs and PG QSOs in this sample. Panel (*c*) shows the distribution of host absolute magnitudes for ULIRGs according to their morphology (black represents dominant early type, hatched corresponds to late type, and white indicates ambiguous systems). Panel (*d*) is the same as panel (*c*) but for the PG QSOs. No obvious trends with dominant morphological type are seen in the data. The vertical dashed line in panels (*b*), (*c*), and (*d*) represents $M_H^* = -23.7$ mags, the H-band absolute magnitude of a L^* galaxy in a Schechter function description of the local field galaxy luminosity function.
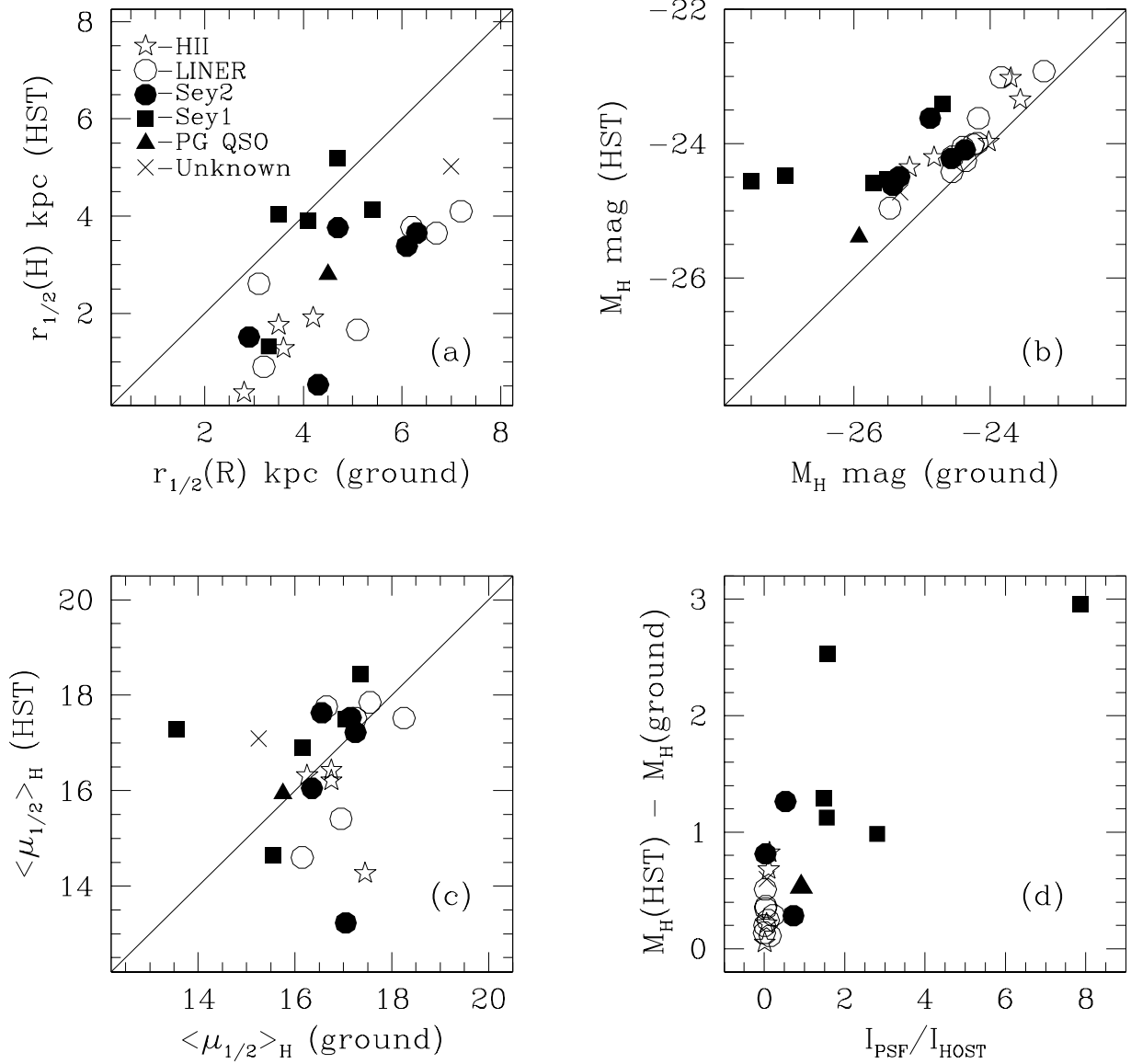
Fig. 8.— Attempt to compare the results from the present H-band study with those from the R-band study of VKS02. (a) half-light radii, (b) host absolute magnitudes, (c) average surface brightnesses within half-light radius. Part of the discrepancies in host sizes may be due to radial color gradients (see text). A color typical of elliptical galaxies at $z \simeq 0.15$ is assumed (R – H = 2.7 mag.) when comparing the magnitudes and surface brightnesses from the two studies. Some of the discrepancies in surface brightnesses and magnitudes may be due in part to this choice of color. However, panel (d) shows that the discrepancies in the magnitude measurements scale with the strength of the PSF component, therefore suggesting that the PSF component in the R-band data has been under-subtracted.
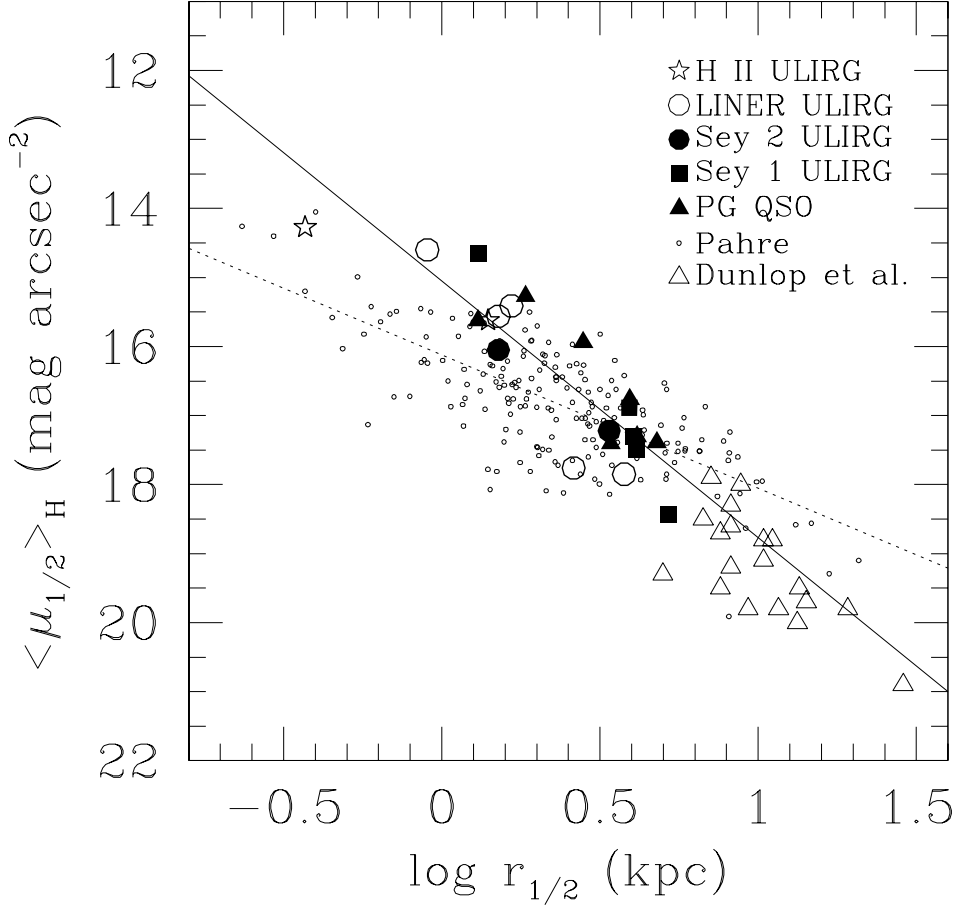
Fig. 9.— Surface brightnesses versus half-light radii for the early-type host galaxies in the *HST* sample. The hosts of the 7 PG QSOs in our sample are statistically indistinguishable from the hosts of the 1-Jy ULIRGs. Both classes of objects fall near the photometric fundamental plane relation of ellipticals as traced by the data of Pahre (1999; dashed line), although the smaller objects in our sample tend to lie above this relation (the solid line is a linear fit through our data points). This may be due to excess H-band emission from a young stellar population. ULIRGs and PG QSOs populate the region of the photometric fundamental plane of intermediate-size ($\sim 1 - 2\ L^*$) elliptical/lenticular galaxies. In contrast, the hosts of the luminous quasars of Dunlop et al. (2003) are massive ellipticals which are significantly larger than the hosts of ULIRGs and PG QSOs. For this comparison, the R-band half-light radii tabulated in Dunlop et al. were taken at face value, and the surface brightnesses in that paper were shifted assuming R – H = 2.9, which is typical for early-type systems at $z \sim 0.2$ (see text for more detail).
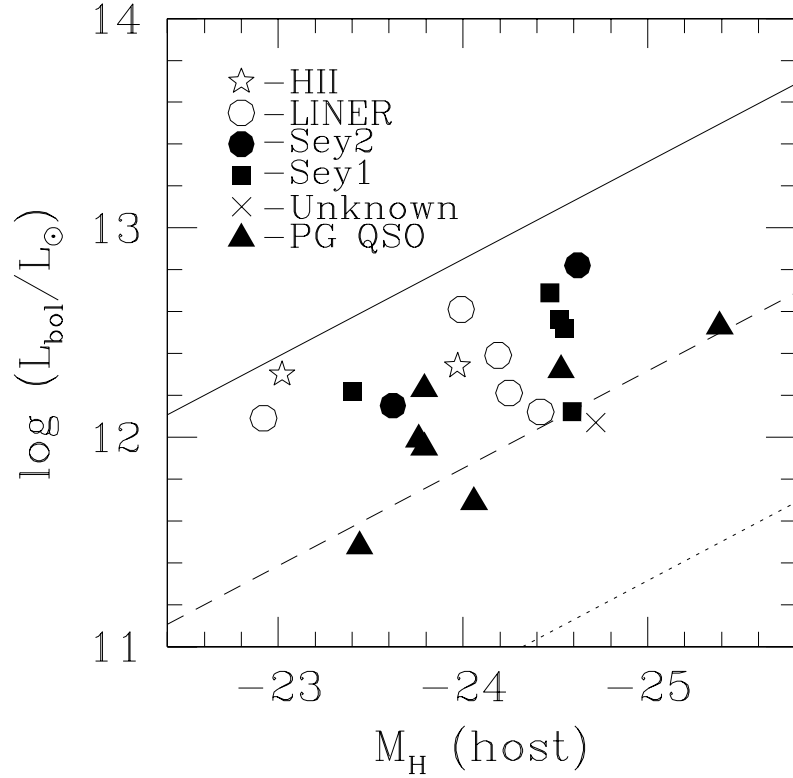
Fig. 10.— Total bolometric luminosities of ULIRGs and PG QSOs with dominant early-type hosts versus absolute magnitudes of the spheroidal components. Diagonal dotted, dashed, and solid lines represent 1%, 10%, 100% of the Eddington luminosity using the relation of Marconi & Hunt (2003) to translate spheroid magnitudes into black hole masses. The Eddington ratios derived from this figure should be considered upper limits since starbursts may contribute an important fraction of the energy in some of these objects, especially those classified as H II galaxies and LINERs. None of the objects in the sample radiate at super-Eddington rates.